MANF regulates neuronal survival and UPR through its
þÿ E R - l o c a t e d   r e c e p t o r   I R E 1 ±

Kovaleva, Vera

2023-02-28

Kovaleva , V , Yu , L , Ivanova , L , Shpironok , O , Nam , J , Eesmaa , A , Kumpula , E-P T ,
Sakson , S , Toots , U , Ustav , M , Huiskonen , J T , Lindholm Pulkkila , P , Voutilainen , M ,
Karelson , M & Saarma , M 2023 , ' MANF regulates neuronal survival and UPR through its
þÿ E R - l o c a t e d   r e c e p t o r   I R E 1 ± ' ,   C e l l   R e p o r t s ,   v o l .   4 2 ,   n o .   2 .   h t t p s : / / d

MANF regulates neuronal survival and UPR through its ER-located receptor IRE1α

Graphical abstract

Highlights

- MANF interacts with IRE1α and competes with BiP for binding to IRE1α

- MANF regulates the activity of IRE1α and its downstream signaling

- MANF interaction with IRE1α is crucial for its pro-survival activity in neurons

- In the rodent model of PD, the neuroprotection by MANF occurs through IRE1α binding
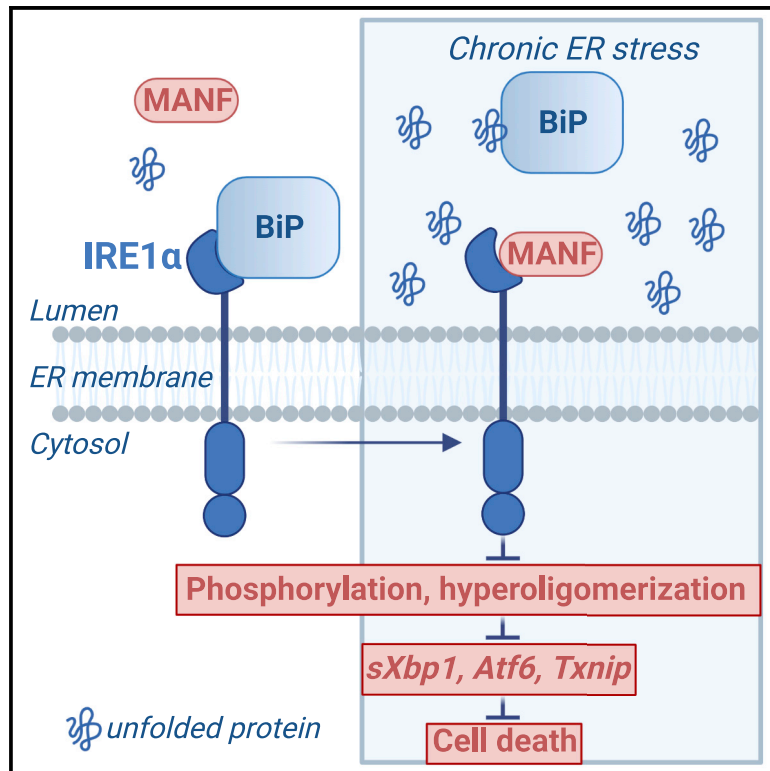
Authors

Vera Kovaleva, Li-Ying Yu,
Larisa Ivanova, ..., Päivi Lindholm,
Mati Karelson, Mart Saarma

Correspondence

vera.kovaleva@helsinki.fi (V.K.),
mart.saarma@helsinki.fi (M.S.)

In brief

Kovaleva et al. show that MANF interacts with UPR sensor IRE1α and negatively regulates its activity upon ER stress. MANF-IRE1α interaction is crucial for survival-promoting action of MANF in neurons and in a rodent model of Parkinson's disease.

CellPress

Cell Reports

Article

MANF regulates neuronal survival and UPR through its ER-located receptor IRE1α

Vera Kovaleva,[1,*] Li-Ying Yu,[1,5] Larisa Ivanova,[2,5] Olesya Shpironok,[1,5] Jinhan Nam,[1,3] Ave Eesmaa,[1] Esa-Pekka Kumpula,[1] Sven Sakson,[1] Urve Toots,[4] Mart Ustav,[4] Juha T. Huiskonen,[1] Merja H. Voutilainen,[1,3] Päivi Lindholm,[1] Mati Karelson,[2] and Mart Saarma[1,6,*]

[1]Institute of Biotechnology, HiLIFE, University of Helsinki, 00014 Helsinki, Finland
[2]Institute of Chemistry, University of Tartu, 50411 Tartu, Estonia
[3]Division of Pharmacology and Pharmacotherapy, Faculty of Pharmacy, University of Helsinki, 00014 Helsinki, Finland
[4]Icosagen Ltd., 61713 Tartu, Estonia
[5]These authors contributed equally
[6]Lead contact
*Correspondence: vera.kovaleva@helsinki.fi (V.K.), mart.saarma@helsinki.fi (M.S.)
https://doi.org/10.1016/j.celrep.2023.112066

SUMMARY

Mesencephalic astrocyte-derived neurotrophic factor (MANF) is an endoplasmic reticulum (ER)-located protein with cytoprotective effects in neurons and pancreatic β cells *in vitro* and in models of neurodegeneration and diabetes *in vivo*. However, the exact mode of MANF action has remained elusive. Here, we show that MANF directly interacts with the ER transmembrane unfolded protein response (UPR) sensor IRE1α, and we identify the binding interface between MANF and IRE1α. The expression of wild-type MANF, but not its IRE1α binding-deficient mutant, attenuates UPR signaling by decreasing IRE1α oligomerization; phosphorylation; splicing of *Xbp1*, *Atf6*, and *Txnip* levels; and protecting neurons from ER stress-induced death. MANF-IRE1α interaction and not MANF-BiP interaction is crucial for MANF pro-survival activity in neurons *in vitro* and is required to protect dopamine neurons in an animal model of Parkinson's disease. Our data show IRE1α as an intracellular receptor for MANF and regulator of neuronal survival.

INTRODUCTION

The endoplasmic reticulum (ER) is the largest intracellular compartment in most eukaryotic cells, dealing with protein secretion and folding as well as lipid biosynthesis and calcium homeostasis. Overloading ER with unfolded or misfolded proteins activates a signaling machinery called unfolded protein response (UPR).[1] Although UPR aims at restoring cellular homeostasis through triggering of pro-survival signaling cascades, its chronic activation leads to apoptosis. UPR in mammalian cells occurs through three ER transmembrane sensors: IRE1α (inositol-requiring enzyme 1α), PERK (PKR-like ER kinase), and ATF6 (activating transcription factor 6).[1]

The IRE1 branch of UPR is the most evolutionarily conserved.[2] A major ER chaperone binding immunoglobulin protein (BiP) is thought to prevent IRE1α activation and signaling in basal conditions.[3] IRE1α is a transmembrane receptor, possessing both serine-threonine kinase and endoribonuclease activities. Upon ER stress BiP dissociation from IRE1α leads to the dimerization of IRE1α luminal domains (IRE1α LDs), trans-autophosphorylation of cytoplasmic domains, increasing IRE1α endoribonuclease activity,[4] which triggers unconventional splicing of X-box-binding protein 1 (XBP1) mRNAs and mRNA decay.

Mesencephalic astrocyte-derived neurotrophic factor (MANF)[5] is an evolutionary conserved ER-located but also secreted unconventional neurotrophic factor.[6] MANF protects and restores dopamine (DA) neurons in an animal model of Parkinson's disease (PD)[7] and also pancreatic insulin-producing β cells *in vivo*.[8,9] Recent data also show that MANF is a key regulator of metabolic and immune homeostasis in aging.[10] Moreover, MANF protects against liver inflammation and fibrosis, suggesting a therapeutic application for MANF in age-related metabolic diseases.[10] MANF is upregulated under ER stress, bypassing general attenuation of protein synthesis.[11]

MANF protects ER-stressed cells and alleviates UPR in a number of *in vitro* models, which indicates that UPR pathways are involved in the pro-survival action of MANF.[11–16]

MANF was proposed to be a negative regulator of the IRE1 pathway in *C. elegans*.[17] In MANF-deficient mice, UPR pathways are chronically activated in pancreatic β cells, neurons, anterior pituitary, and liver, demonstrating that MANF is a crucial regulator of UPR *in vivo*.[8,9,15,18] Interestingly, MANF knockout mice have a diabetic-like phenotype similar to IRE1α or XBP1 knockout mice. All three knockout models have endocrine pancreas alterations, altered glucose metabolism and insulin secretion, as well as lipid abnormalities in the liver.[8–10,19,20]

These data provide genetic evidence for MANF and IRE1α being involved in similar functions and signaling pathways. MANF-IRE1α crosstalk is further supported by the notion that in MANF knockout mice the IRE1α branch of the UPR is activated first, and PERK and ATF6 pathways are activated later.[8] The same was observed for pancreas-specific[9] and central nervous system-specific MANF ablation.[15]

The exact mechanism of IRE1α activation remains unclear. Several mutually exclusive modes of IRE1α activation were described.[21–26] Unfolded proteins and chaperones were shown to play a role in the regulation of IRE1α activation.[27,28] To date, the exact mode of action of MANF also remains poorly understood. In human and mouse pancreatic β cells, and also in neurons, MANF is mostly localized inside the cells in the ER,[18,29,30] implying that ER is its main site of action. In line with this, MANF added extracellularly to superior cervical ganglion (SCG) neurons had no pro-survival effect, but when the plasmid encoding MANF or MANF protein were microinjected they protected the neurons from ER stress-induced apoptosis.[16,29] However, in cultured human and mouse pancreatic β cells MANF added extracellularly has a clear cytoprotective[9,30,31] and proliferative effect,[8] showing that MANF can act via its plasma membrane receptors or enter the cells, translocate to the ER and act there. Thus, the pro-survival action of extracellularly added MANF is likely cell type specific. Recently, neuroplastin was identified as a plasma membrane receptor of MANF, involved in the regulation of MANF-mediated attenuation of inflammation.[32] MANF interacts with the major ER chaperone BiP[33] and other chaperones, including PDIA6 and GRP170.[16,34] Recently, MANF was shown to prolong the interaction of BiP with its client proteins, thus regulating protein-folding homeostasis.[35] However, we demonstrated that the interaction with BiP was not required for the pro-survival activity of MANF.[16]

Here, we show that MANF directly binds to IRE1α with high affinity, competes with BiP for the interaction with IRE1α, and regulates UPR through direct interaction with IRE1α. This interaction inhibits the activity of IRE1α by regulating its oligomerization, phosphorylation, and downstream signaling. IRE1α non-binding mutant of MANF is unable to regulate IRE1α activity, lacks pro-survival effect *in vitro* in SCG and DA neurons, and is inactive *in vivo* in an animal model of PD. Complementary IRE1α LD mutagenesis confirmed the binding of MANF to the oligomerization site of IRE1α LD. Thus, our results reveal the mode of action of MANF in the ER and bring to light MANF as a regulator of IRE1α activity.

RESULTS

MANF directly interacts with the LD of IRE1α

The LDs of all three human UPR sensors, IRE1α, PERK, and ATF6, were expressed and purified from mammalian CHO cells (Figure S1A). We demonstrated that N-linked glycosylation was absent in IRE1α LD and PERK LD and, as reported earlier,[36] present in ATF6 LD (Figure S1A). To assess the biological activity of purified UPR sensor LDs we tested their interactions with BiP using microscale thermophoresis (MST). We found that BiP interacted with fluorescently labeled UPR sensors with high affinities (Figures 1A–1C; Table S1). Notably, the affinities of BiP for these

mammalian cell-produced proteins were about 10–100 times higher than those reported for those produced by *E. coli*.[24]

We tested the interaction between mammalian UPR sensor LDs and MANF using MST, and found that MANF interacts with all three UPR sensors, the highest affinity being observed for MANF-IRE1α LD interaction (Figure 1D; Table S1). MANF interacted with PERK and ATF6 LDs with lower affinities (Figures 1E and 1F; Table S1).

Taking into account the higher affinity of MANF to IRE1α LD, as compared with PERK and ATF6 LDs, we further focused on the MANF-IRE1α LD interaction, and tested it using two other methods. In gel filtration chromatography, MANF and IRE1α LD co-eluted revealing that MANF interacts with the monomer of IRE1α LD (Figure S1B). Furthermore, the binding of MANF and IRE1α LD-His on nickel-coated plates also confirmed their direct interaction (Figure S1C).

BiP prevents MANF interaction with IRE1α LD

Both MANF and BiP were able to bind IRE1α LD with similar affinities. Therefore, we hypothesized that BiP can prevent the interaction between MANF and IRE1α LD if MANF and BiP have the overlapping binding site on IRE1α LD. Alternatively, MANF binding to BiP could increase the affinity of BiP interaction with IRE1α allosterically if they form a tripartite complex. To distinguish between these two models, the interactions between MANF and IRE1α LD in the presence of increasing concentrations of BiP (1–50 nM) were tested using MST. BiP (10 nM) decreased the affinity of MANF binding to IRE1α LD and 50 nM BiP abolished the interaction (Figure 1G), suggesting that MANF and BiP could compete for the overlapping binding site in IRE1α LD.

Interestingly, in the presence of increasing concentrations of MANF (10 nM to 1 μM), BiP was still interacting with IRE1α LD (Figure S1D). An unphysiological 10 μM concentration of MANF abolished the BiP-IRE1α LD interaction (Figure 1H). Thus, likely MANF binds IRE1α LD only when BiP dissociates to bind misfolded or aggregated proteins upon ER stress.[3]

Ca²⁺ regulates MANF-IRE1α LD interaction

Considering that ER is crucial for maintaining cellular calcium homeostasis and that Ca^{2+} depletion from ER is known to activate the UPR, we tested whether Ca^{2+} affects the MANF interaction with UPR sensors. The concentration of free Ca^{2+} in ER has been reported to be between 100 μM and 1–3 mM, depending on the measurement techniques and cell types used.[37] We found that, in the presence of 500 μM Ca^{2+}, the affinity of MANF to IRE1α LD was slightly decreased and no changes in the affinities of MANF to PERK and ATF6 LDs were observed (Figures S1E–S1G). When we tested the MANF-IRE1α LD interaction further in the presence of increasing concentrations of Ca^{2+} (100 μM to 2.5 mM), we found that the affinity of MANF to IRE1α was inversely proportional to Ca^{2+} concentration (Figures 1I and 1J).

C-MANF directly interacts with IRE1α LD

Since the 63 amino acid C-terminal domain of MANF (C-MANF) can protect neurons as efficiently as full-length MANF,[14] we hypothesized that binding of MANF to IRE1α may occur through C-MANF. We tested the interactions between chemically
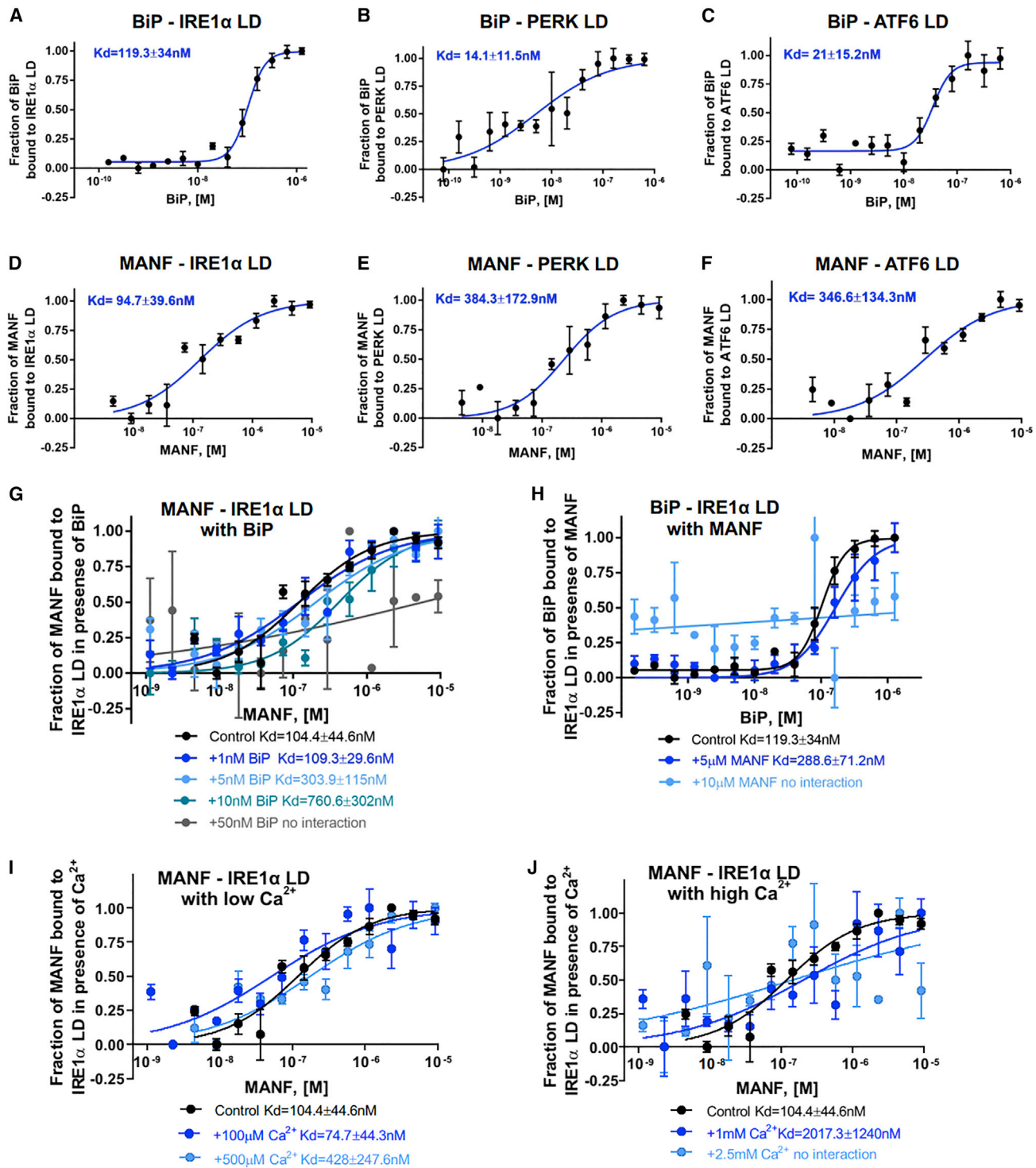
Figure 1. MANF directly interacts with IRE1α LD, and BiP is preventing MANF interaction with IRE1α LD

(A–C) BiP (0–640 nM) interacts with labeled (A) IRE1α, (B) PERK, and (C) ATF6 LDs.

(D–F) MANF (0–9.3 μM) interacts with labeled (D) IRE1α, (E) PERK, and (F) ATF6 LDs.

(G) MANF (0–9.3 μM) interaction with labeled IRE1 LD is affected by BiP (1–50 nM).

(H) BiP (0–640 nM) interaction with labeled IRE1α LD is affected by 5 or 10 μM of MANF.

(I) Interaction of MANF (0–9.3 μM) with labeled IRE1α LD in the presence of low concentrations of Ca^{2+} (100 and 500 μM).

(J) Interaction of MANF (0–9.3 μM) with labeled IRE1α LD in the presence of high concentrations of Ca^{2+} (1 and 2.5 mM). In (A)–(J) the labeled targets were used at 20 nM. MST binding curves, showing mean fraction bond values from n = 3–5 experiments per binding pair ± SEM. K_d values ± error estimations are indicated.

A

GFP-HA-MANF   IRE1α-HA-MANF

B
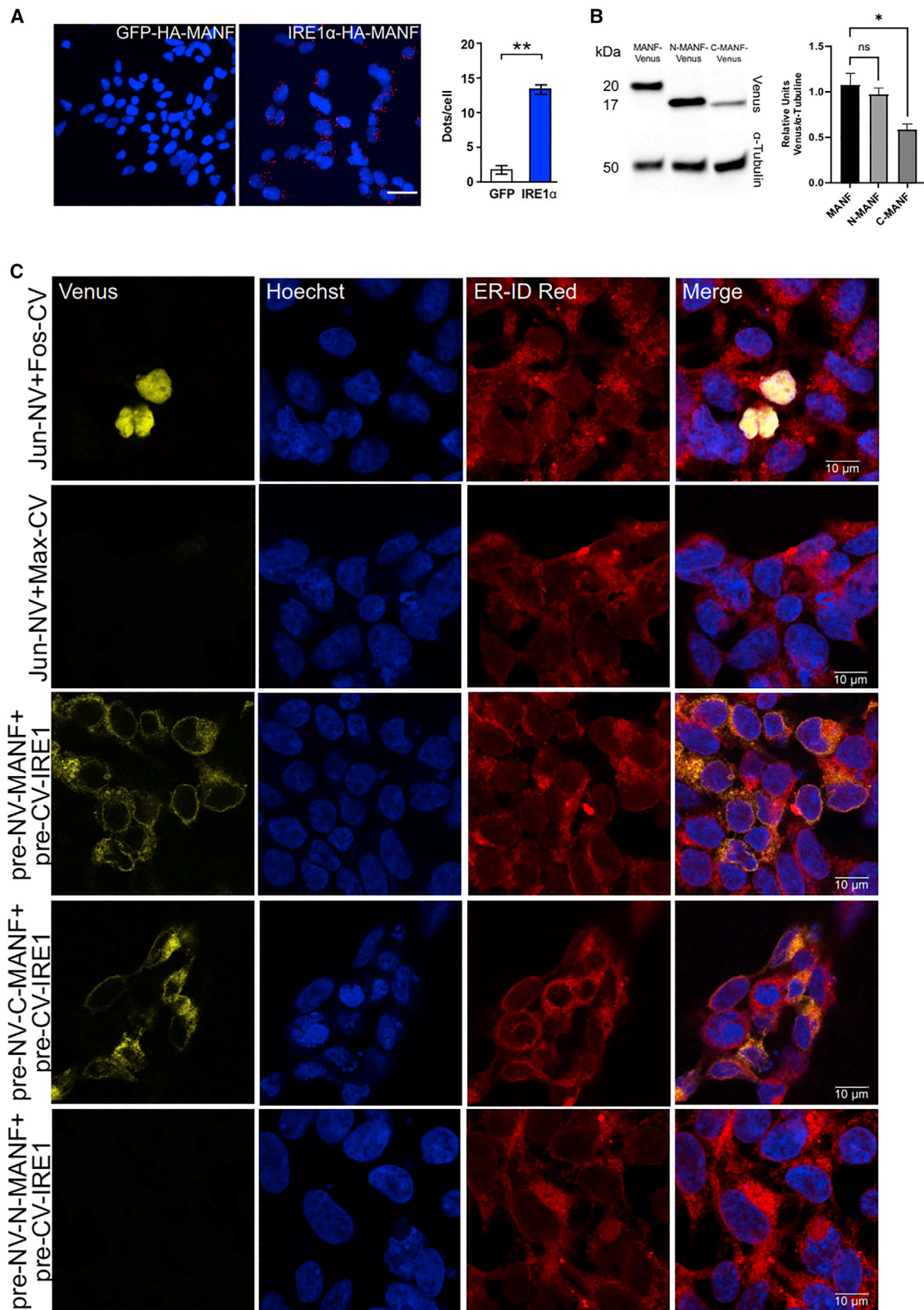
(legend on next page)

synthesized or bacterially expressed C-MANF (K96-L158) with IRE1α, PERK, and ATF6 LDs as was done for full-length MANF. We showed that chemically synthesized C-MANF interacts with all three UPR sensors with higher affinities compared with full-length MANF (Figures S1H–S1J). We also demonstrated that chemically synthesized C-MANF is homogeneous, similarly to the C-terminal domain of full-length MANF, has a disulfide bond, and is biologically active in SCG neurons (Figure S1K). Bacterially expressed C-MANF also interacted with UPR sensors, but the affinities were significantly lower compared with full-length MANF and chemically synthesized C-MANF, likely due to the absence of disulfide bonds. As with full-length MANF, bacterially produced C-MANF also had the highest affinity to IRE1α LD and lower affinities to PERK and ATF6 LDs (Figures S1L–S1N).

MANF interacts with IRE1α LD in cells

To test whether the interaction between MANF and IRE1α occurs in cells, we performed an *in situ* proximity ligation assay in Flp-In-T-REx 293 and CHO cells. We found that in Flp-In-T-REx 293 cells endogenous MANF interacted with IRE1α-HA (Figure 2A). The interactions between MANF and BiP-HA and GFP-HA in corresponding cell lines served as positive and negative controls, respectively. In addition, we demonstrated that endogenous IRE1α interacts with MANF-HA in CHO cells (Figure S2A). In a cell line expressing a truncated version of MANF (MANF Δ110–158), lacking a part of the C-MANF, the interaction between MANF-HA and IRE1α was compromised (Figure S2A).

We further demonstrated that pre-NV-MANF is interacting with pre-CV-IRE1α LD in HEK293 cells using bimolecular fluorescence complementation (BiFC) assay (Figure 2C). In line with MST experiments, we found that the interaction between MANF and IRE1α LD in cells also occurs through C-MANF. Moreover, the N-terminal domain of MANF (N-MANF) showed no interaction with IRE1α LD (Figure 2C). Since the N-MANF does not have an ER retention signal, likely it can be secreted more quickly than MANF and C-MANF. To address this potential caveat we tested the expression level N-MANF using western blotting (WB) and found that it is expressed at the same level as MANF (Figure 2B). We also found that C-MANF was expressed at a lower level than full-length protein and N-MANF, likely due to its quicker degradation (Figure 2B). N-MANF was localized to the ER, similarly to MANF and C-MANF, as assessed using immunocytochemistry (Figure S2B).

In addition, we tested the interaction of the BiP nucleotide-binding domain (BiP NBD) and BiP substrate-binding domain (BiP SBD) with IRE1α LD. According to our data, BiP mainly interacts with IRE1α LD through its NBD, and not through BiP SBD (Figure S2C).

## Endogenous MANF and IRE1α reside in a protein complex

MANF knockdown using small interfering RNA oligos targeting *MANF* resulted in an average decrease of 50% in the level of MANF in HEK293 cells and a significant upregulation of IRE1α, indicating crosstalk between the regulation of endogenous MANF and IRE1α expression (Figure 3A). To study the molecular interaction between endogenous MANF and IRE1α we stabilized protein-protein interactions in HEK293 cells using chemical crosslinking and collected MANF protein complexes by co-immunoprecipitation (co-IP). HEK293 cells endogenously express MANF, IRE1α, and BiP (Figure 3B; input). After crosslinking, IRE1α was detected in MANF co-IP complex, indicating that MANF and IRE1α can physically interact in cells (Figure 3B). Without crosslinking, IRE1α was not detected in the MANF co-IP complex, suggesting that the MANF-IRE1α interaction is labile and transient in nature (Figure 3B). Similarly to previous studies,[16,33,35] BiP was detected in the MANF co-IP complex (Figure 3B). Negative controls demonstrated the specificity of MANF antibodies used in the co-IP reactions (Figure S3A).

To study how acute and chronic ER stress affects interaction dynamics of endogenous MANF, IRE1α, and BiP, we treated HEK293 cells with tunicamycin (TM) and thapsigargin (TG) for 1, 4, and 20 h, and analyzed crosslinked MANF co-IP complexes using WB. TM treatment-induced transient phosphorylation of IRE1α was evident at 4 h while it was decreased by 20 h (Figure 3C, input). TM treatment for 20 h induced upregulation of MANF, IRE1α, and BiP, indicating chronic ER stress and UPR activation in the cells (Figures S3B–S3D). In all time points, IRE1α was detected in the MANF co-IP complex (Figure 3C), indicating that MANF and IRE1α reside in a complex both in acute and chronic ER stress. IRE1α levels in the MANF co-IP complex did not significantly differ between the time points of TM treatment (Figure 3D), while BiP was significantly increased in the complex after 20 h of TM treatment (Figure 3E). This suggests that more BiP is present in a complex together with MANF and IRE1α in chronic vs. acute TM-induced ER stress.

Resembling effects of TM in HEK293 cells, TG treatment for 1 and 4 h induced transient activation of the IRE1α pathway, which was decreased after 20 h (Figure 3F). TG treatment for 20 h induced upregulation of MANF, IRE1α, and BiP, indicating chronic ER stress and UPR activation (Figures S3E–S3G). We detected IRE1α in crosslinked MANF co-IP complexes at 1, 4, and 20 h of TG treatment (Figure 3F). The level of IRE1α in the MANF co-IP complex was increased at 20 h compared with the shorter treatments (Figure 3G), suggesting that more IRE1α is present in the MANF co-IP complex in chronic, TG-induced ER stress than in acute ER stress. Differently from IRE1α, BiP was not significantly increased in the MANF co-IP complex after 20 h of TG treatment, although its level showed an increasing trend (Figure 3H).

Figure 2. MANF interacts with IRE1α in cells
(A) Left: representative image of MANF-IRE1α-HA interaction, as demonstrated using proximity ligation assay. GFP-HA was used as a negative control. Scale bar, 20 μm. Right: quantification of dots/cell for MANF-IRE1α-HA vs. MANF-GFP-HA interaction. Mean dots/cell ± SEM; n = 3. Student's t test; **p < 0.01.
(B) Estimation of the expression level of Venus constructs of MANF, N-MANF, and C-MANF for bimolecular fluorescence complementation (BiFC) assay in HEK293 cells using WB. A representative image is on the left and quantification is on the right. Venus level was normalized to α-tubulin level, n = 3. One-way ANOVA, Tukey's post hoc test. *p ≤ 0.05; ns, not significant.
(C) MANF interacts with IRE1α through its C-terminal domain, but not N-terminal domain in HEK293 cells, as shown using BiFC, n = 3. Scale bar, 10 μm.
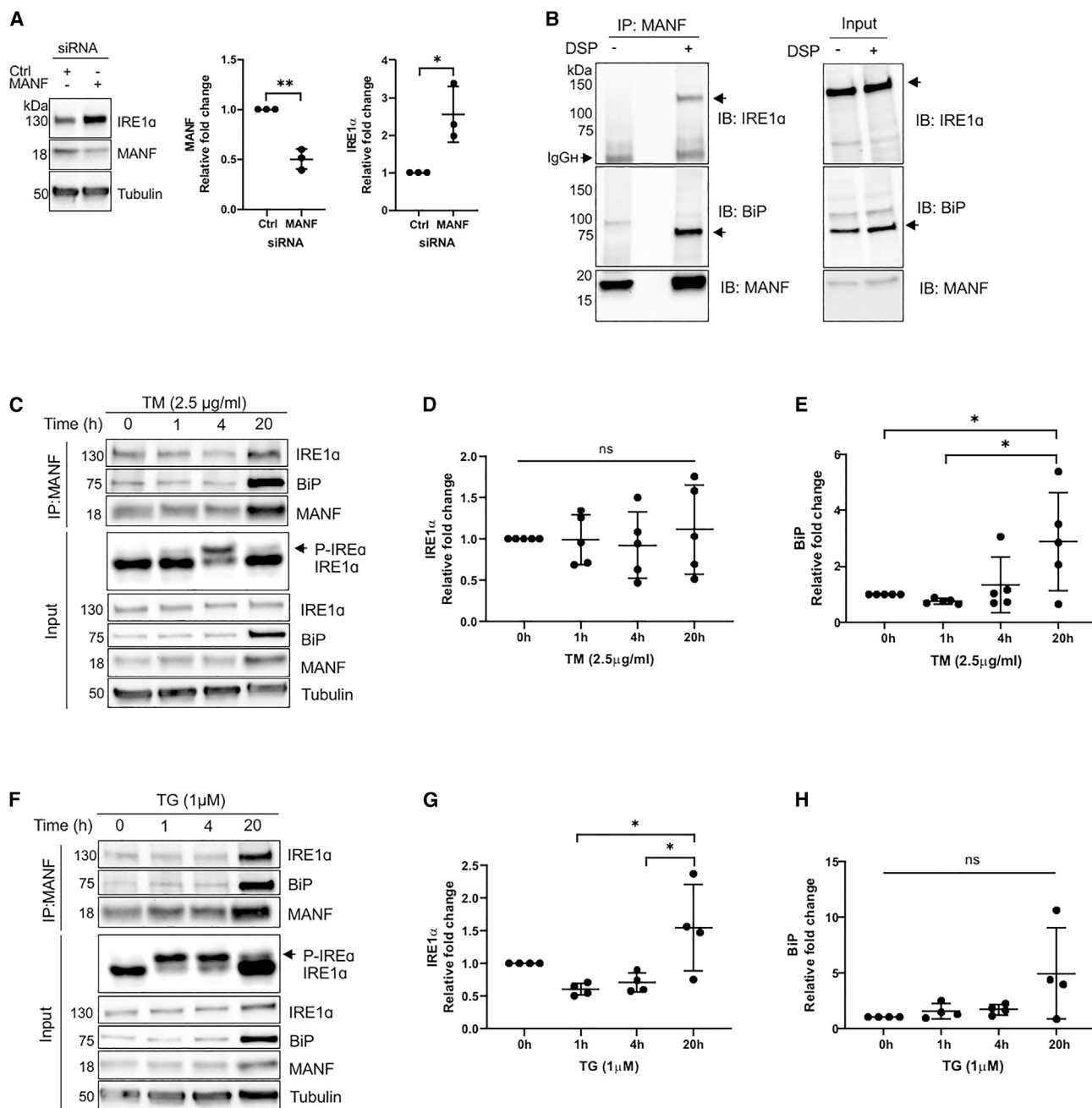
Figure 3. Endogenous MANF and IRE1α interact in HEK293 cells

(A) Knockdown of MANF upregulates IRE1α. Cells were transfected with MANF small interfering RNA (siRNA) or no-targeting siRNA as a control, and protein expression was analyzed 48 h later using immunoblotting. Tubulin was used as a loading control. Mean ± SD; n = 3. Student's t test; *p ≤ 0.05, **p ≤ 0.01.

(B) MANF, IRE1α, and BiP reside in a protein complex. After crosslinking, MANF protein complexes were co-immunoprecipitated from cell lysates using anti-bodies to MANF. Proteins were analyzed by immunoblotting (IB) using antibodies to MANF, IRE1α, and BiP. IRE1α and BiP were detected in MANF im-munocomplex. Input samples represent whole lysates. Arrows indicate IRE1α and BiP bands. IgG$_H$, immunoglobulin G heavy chain; IP, immunoprecipitation.

(C–E) Dynamics of IRE1α and BiP in MANF immunocomplex after tunicamycin (TM)-induced ER stress in HEK293 cells. (C) Cells were treated with TM for 1, 4, or 20 h followed by crosslinking and co-immunoprecipitation against MANF. IRE1α and BiP were detected by immunoblotting. TM treatment for 4 h induced phosphorylation of IRE1α (P-IRE1α) as detected using Phos-tag SDS-PAGE. TM treatment for 20 h upregulated IRE1α, BiP, and MANF levels in the cells. (D and E) Quantification of IRE1α and BiP in MANF complex in (C). (D) IRE1α was detected in MANF co-IP complex after short (1 and 4 h) and long (20 h) TM treatment. (E) Increased BiP in MANF co-IP complex after TM treatment for 20 h. Mean ± SD, n = 5.

(F–H) Dynamics of IRE1α and BiP in MANF co-IP complex in thapsigargin (TG)-induced ER stress. (F) HEK293 cells were treated with TG for 1, 4, or 20 h followed by crosslinking and MANF co-IP. Input samples show TG-induced P-IRE1α at 1 and 4 h time points. IRE1α, BiP, and MANF were upregulated after 20 h of TG. (G

(legend continued on next page)

Identification of the IRE1α LD binding site in MANF

To identify the potential binding sites between MANF and IRE1α we used molecular docking calculations[38,39] with known three-dimensional (3D) structures of C-MANF (PDB: 2KVE)[14] and IRE1α LD (PDB: 2HZ6),[40] followed by MANF site-directed mutagenesis and testing of the mutants.

At first, the interactions between C-MANF and IRE1α LD were studied using docking without any mutual protein position constraints. The IRE1α LD was considered to act as a receptor and C-MANF as a ligand being docked flexibly. Thirty computationally generated models of the C-MANF-IRE1α LD complexes (referred to as models) corresponding to different relative positions of C-MANF and IRE1α LD were obtained. The analysis of the protein-protein interactions of the predicted models suggested that IRE1α LD is contacted primarily by the link between C- and N-terminal domains of MANF involving the M94-T105 and by K150-L158 regions (Table S2, models 1–30).

To estimate the importance of individual amino acid residues of C-MANF in the interaction with IRE1α LD, the frequency of the appearance of each residue in all models and the number of models involving hydrogen bonding at the complex interface was counted (Table S3).

We found that M94, K96, and R155 of C-MANF had the most frequent involvement in specific interactions, i.e., the hydrogen bonds, and these residues were proposed as targets for mutations (Figure 4A).

Next, the docking was performed with structural constraints in the C-MANF (Figure 4B). Based on our earlier published data,[29] the cysteine loop in the C-MANF was considered as a putative binding site. We found that the cysteine loop of MANF was involved in interactions between the proteins only in 4 models out of 30 (Table S2). In this analysis, the calculations were performed only for C127, K128, G129, and C130, which were also proposed as targets for mutations (Figure 4C; Table S3).

Further analysis led to the identification of two potential binding sites in C-MANF: region 1 including the link between C- and N-terminal domains and region 2 including the residues of the cysteine loop of MANF (Figure 4D). However, region 2 was predicted only when structural restrictions in C-MANF were applied. Thus, the preferred site for C-MANF binding with IRE1α LD is the link between the C- and N-terminal domains. Notably, these residues in C-MANF are highly evolutionarily conserved (Figure S4A).

Identification of MANF binding site in IRE1α LD

We further focused on the identification of the potential MANF binding site in IRE1α LD (Figure 4E). The analysis of possible MANF binding residues of IRE1α LD was carried out as described above, and four putatively important interaction regions were identified (Figure 4F; Tables S4 and S5). Region 1 includes H67-F73, L85, Q105, and R110; region 2 includes D123, W125, Y155, and E235; region 3 includes V247, E248, R251, Y252, F255, M256, and E259; and region 4 includes K288, H301-V307, W359, and L360 (Table S4). Notably, regions 2 and 4 cover the dimerization and oligomerization sites of IRE1α

LD, respectively.[21] Eight IRE1α LD residues most frequently involved in interaction with MANF were selected for mutations: E69 (region 1), W125, Y155, E235 (region 2), R251, Y252 (region 3), and W359, L360 (region 4). However, since regions 1, 3, and 4 are located on the opposite side to the dimerization site (region 2) of IRE1α LD protein, they can represent a single MANF binding site.

We have generated four IRE1α LD mutants, E69A, W125G, Y252F, and W359G, of putative binding regions 1–4, plus a double mutant W125G W359G of regions 2 and 4, because, based on our findings, described further, we considered these regions important for MANF-IRE1α interaction (Figure 4F). In addition, a double mutant W359G L360S of region 4 of IRE1a LD, and the IRE1α oligomerization deficient mutant W359G L360S L361G I362S described earlier[21] were generated.

The expression levels of all generated IRE1α LD mutants were similar to that of wtIRE1α LD (Figure S4B). Using MST, we found that all IRE1α LD mutants except for the dimerization site mutant IRE1α LD W125G were deficient for MANF binding (Figures 4G–4I).

MANF reduces IRE1α oligomerization upon ER stress

Based on the results of computational modeling, we generated MANF mutants, putatively deficient in IRE1α LD binding, the cysteine loop C130S and K128AC130S, the linker region K96A, and the RTDL sequence R155A MANF mutants. The levels of their expression and secretion were similar to that of the wild-type MANF (wtMANF) (Figure S5A). No changes in the localization of MANF mutants compared with wtMANF were observed using immunocytochemistry in SCG, as was described earlier[29] (Figures S5B and S5C).

We assessed the effect of MANF on the oligomerization of IRE1α using an inducible IRE1α-GFP cell line[41] (Figure S5D). We found that transient 48 h overexpression of MANF decreased the number of IRE1α-GFP foci per cell upon treatment with TM, whereas expression of empty vector had no effect on IRE1α oligomerization (Figure 5A). In addition, we showed that MANF protein added to cultured cells decreased IRE1α oligomerization upon TG treatment and tended to decrease IRE1α oligomerization upon TM treatment (Figures S5E–S5G).

Next, we tested whether MANF mutants putatively deficient for IRE1α binding have a similar effect on the oligomerization of IRE1α as wtMANF. MANF K96A and MANF R155A did not reduce the number of IRE1α-GFP foci (Figure 5B). MANF cysteine loop mutants MANF C130S and MANF K128AC130S decreased IRE1α oligomerization similarly to wtMANF, suggesting that the cysteine loop of MANF is not involved in MANF binding to IRE1α.

We expressed and purified MANF K96A and MANF K128AC130S, putatively deficient for IRE1α binding (Figure S5H). MANF K96A (region 1, Figure 4D) was chosen due to a more pronounced difference from wtMANF activity in the IRE1α oligomerization assay compared with other mutants, and MANF K128AC130S was chosen to test the role of another putative IRE1α-binding region in MANF (region 2, Figure 4D) in

and H) Quantification of IRE1α and BiP in MANF complex (F). (G) IRE1α in MANF co-IP complex was upregulated after 20 h TG treatment. (H) No significant differences in BiP level during TG-induced ER stress. Mean ± SD, n = 4. In (D), (E), (G), and (H) IRE1α and BiP signal is normalized to MANF. One-way ANOVA, Tukey's post hoc test. *p ≤ 0.05; ns, not significant.
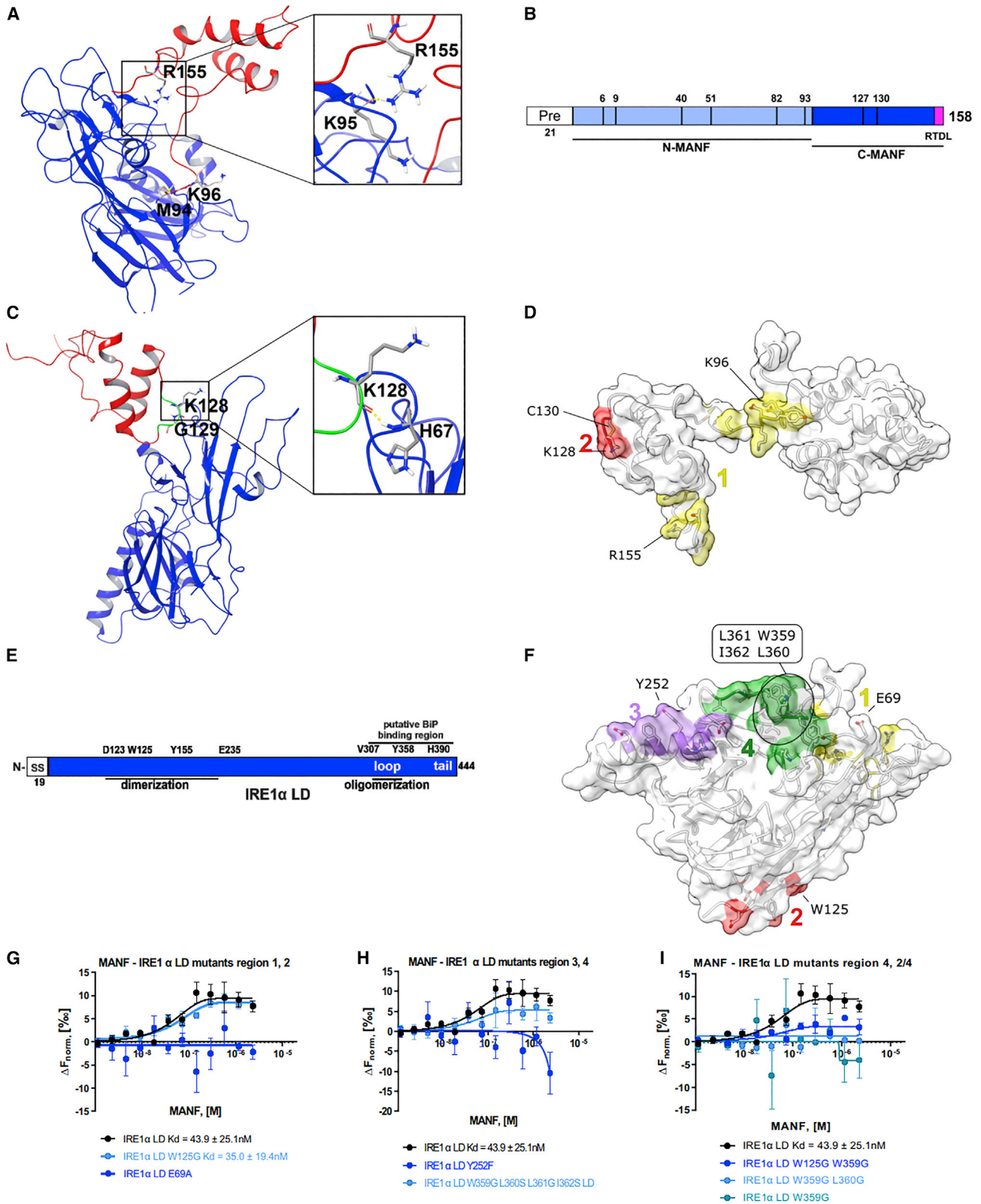
(legend on next page)

MANF-IRE1α binding. Using MST, we found that, while MANF K96A was not interacting with fluorescently labeled IRE1α LD, the affinity of MANF K128AC130S to IRE1α LD was similar to that of wtMANF (Figure 5C).

We further tested the MANF effect on IRE1α oligomerization in MST. First, we demonstrated that IRE1α LD is interacting with fluorescently labeled IRE1α LD (Figure 5D). Next, we demonstrated that, in the presence of 1 μM MANF, the affinity of IRE1α LD to IRE1α LD does not significantly change, but in the presence of 5 μM MANF the IRE1α LD-IRE1α LD interaction is abolished (Figure 5D), confirming the ability of MANF to decrease IRE1α oligomerization. We found that in the presence of MANF K96A IRE1α LD is still binding IRE1α LD with similar affinities as without MANF K96A (Figure 5E). This finding suggests that the direct binding of MANF to IRE1α LD is crucial for MANF's ability to decrease IRE1α oligomerization.

Role of the oligomerization site of IRE1a LD in interaction with MANF

To evaluate the role of oligomerization and dimerization sites of IRE1α LD in interaction with MANF, homology modeling of the full-length structure of IRE1α LD using the SWISS-MODEL server[42,43] was carried out since residues V308-N357 belonging to the oligomerization site of IRE1α LD (region 4) are not resolved in the available crystal structure of IRE1α LD.[40] Using the full-length structures of IRE1α LD (model 1, Figure S4C) and wtMANF (PDB: 2W51),[44] we demonstrated that MANF contacted IRE1α LD primarily in the area between the C- and N-terminal domains of the MANF with the involvement of residues from the C-terminal (P145-L158) and N-terminal (R41-D59) domains. Notably, in line with our experimental data, more contacts and hydrogen bonds in predicted models of the wtMANF-IRE1α LD complex were observed for C-MANF residues compared with N-MANF (Table S6, models 61–90). The analysis of wtMANF-IRE1α LD complex led to the identification of four potential binding regions in IRE1α LD (Figure 4F), as in the case of docking using the available 3D structures. In addition, the analysis of the docking results showed that the residues of the IRE1α LD region not resolved in the crystal structure (V308-N357) are also involved in the interaction between wtMANF and IRE1α LD (Table S6). For further study of the role of oligomerization sites and the role of the flexible region IRE1α LD in the interaction with MANF, additional protein-protein docking with full-length MANF K96A and MANF R155A (Table S7) mutants was carried out. The MANF K96A

and MANF R155A mutants were generated by a residue mutation procedure using Schrödinger Maestro software (Schrödinger Release 2018-3: Maestro, Schrödinger, NY). In the case of MANF K96A, the greatest changes affect the residues belonging to the flexible region of IRE1α LD (Table S7). Namely, for L313-L316 of IRE1α LD, the number of predicted models in which these residues are involved in binding to the MANF K96A is significantly reduced compared with wtMANF, and the E317-P319 residues of IRE1α LD are no longer involved in the binding to MANF K96A. In the case of MANF R155A, the greatest changes were also observed for the L313-P319 residues of IRE1α LD (Table S7). Thus, region 4 of IRE1α LD can be considered more likely to be involved in MANF-IRE1α LD interaction.

## MANF reduces IRE1α phosphorylation and attenuates the level of sXbp1 mRNA upon ER stress

We further tested the effect of MANF on IRE1α phosphorylation, and found that MANF treatment of MEFs reduced pSer724-IRE1α level upon ER stress (Figure 6A).

We used qRT-PCR analysis to analyze how MANF and MANF mutants affect signaling downstream of UPR sensors. We found that exogenously added MANF reduced the mRNA level of sXbp1 and that MANF K128AC130S also tended to reduce it upon TM-induced ER stress in MEFs (Figure 6B). The MANF K96A deficient for IRE1α LD binding failed to decrease the mRNA level of sXbp1 (Figure 6B). We also found that MANF decreased the level of Txnip (p = 0.056) and both MANF K96A and MANF K128AC130S were not affecting the Txnip level (Figure 6C). In addition, we tested whether MANF or MANF mutants affect BiP, Chop, Atf6, and tXbp1. No significant changes in the mRNA levels of these UPR markers were found (Figures S6A–S6D).

We performed a similar analysis of downstream UPR sensor signaling in DA neurons upon TG-induced ER stress. MANF decreased the levels of sXbp1 and Atf6, while MANF K96A was not affecting them (Figure 6D). MANF tended to decrease also other UPR genes tested and MANF K96A was not affecting them (Figure 6D). We further tested whether IRE1α inhibition using 4μ8C or KIRA6 affected the effect of MANF on UPR genes in DA neurons. We found that the IRE1α inhibition with 4μ8C or KIRA6 abolished MANF-induced downregulation of tXbp1. The downregulation of sXbp1 and Atf6 was still significant; however, less pronounced than without IRE1α inhibition (Figure S6E).

Figure 4. Putative MANF-IRE1α binding sites identified using protein-protein molecular docking

(A) Relative position of MANF (red ribbons) and IRE1α LD (blue ribbons) proteins in model 12. The hydrogen bond between R155 of MANF and K95 of IRE1α is represented as a yellow dashed line.

(B) Scheme of two-domain MANF structure.

(C) Relative position of MANF (red ribbons) and IRE1α LD (blue ribbons) proteins in model 41. The cysteine loop of the MANF is given in green color, hydrogen bond is represented as yellow dashed line.

(D) Putative IRE1α LD binding regions 1 and 2 in full-length MANF (PDB: 2W51) are colored in red and yellow, respectively. Mutated amino acids are indicated.

(E) Scheme of IRE1α LD with important structural parts indicated.

(F) Putative MANF binding regions 1, 2, 3, and 4 in IRE1α LD (PDB: 2HZ6) are colored in yellow, red, green, and purple, respectively. Mutated amino acids are indicated.

(G–I) Labeled IRE1α LD mutants, mutated in region 1 (E69A), region 3 (Y252F), region 4 (W359G, W359G L360G, W359G L360G L361G I362S), and region 2 + region 4 (W125G W359G) (20 nM) are not interacting with MANF (0–2.3 μM), while the affinity of IRE1α region 2 mutant (W125G) is the same to that of wtIRE1α LD protein. MST binding curves, showing mean ΔF_{norm} values from n = 3–5 repeats per binding pair ± SEM. K_d values ± error estimations are indicated.
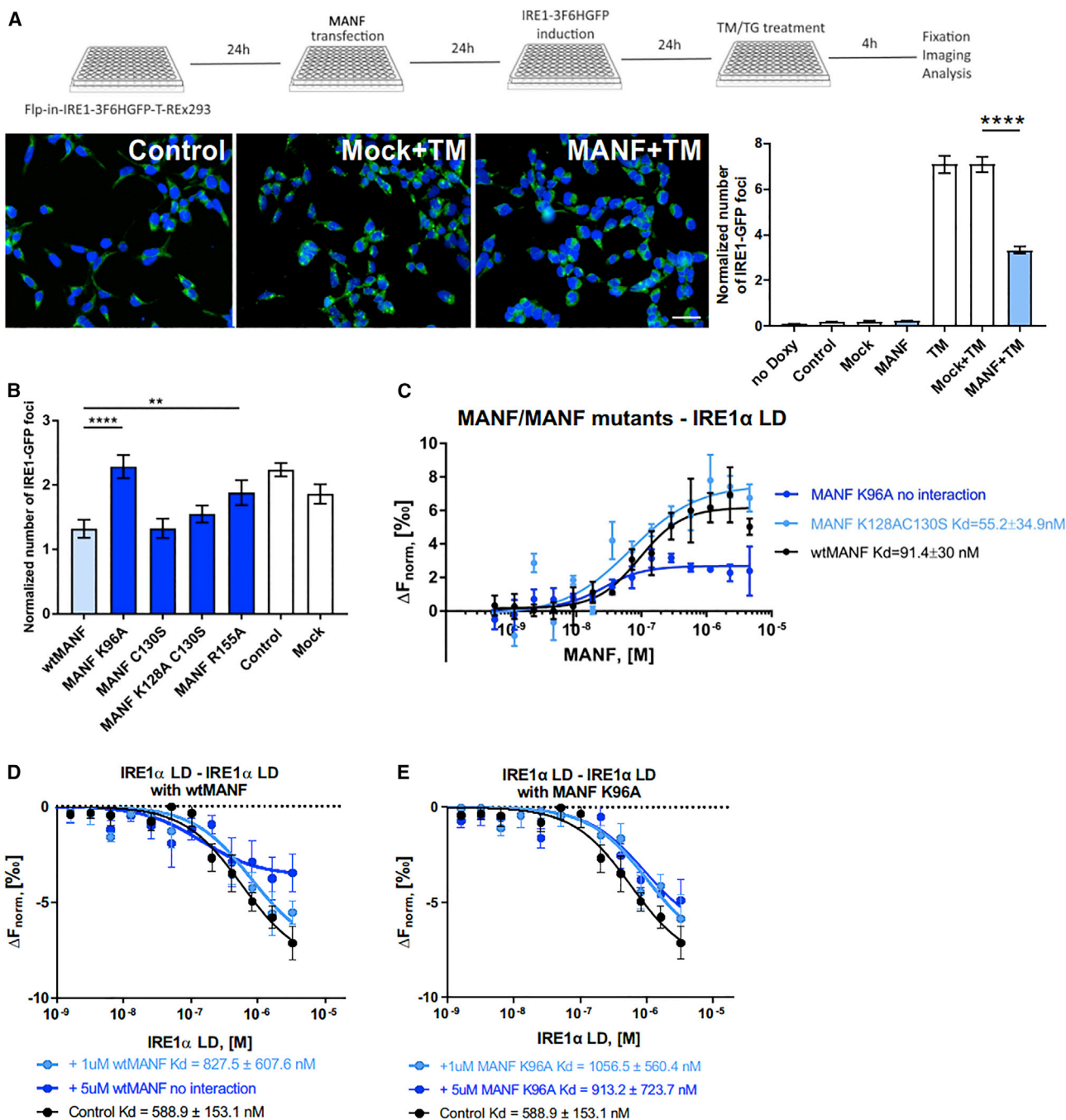
Figure 5. MANF decreases IRE1α oligomerization and IRE1α binding-deficient MANF mutant does not affect IRE1α oligomerization upon ER stress

(A) MANF overexpression decreases ER stress-induced IRE1α oligomerization, as shown using an IRE1α-3F6HGFP-inducible cell line. Scale bar, 100 μm. One-way ANOVA, Dunnett's post hoc test, n = 3; ****p < 0.0001.

(B) The overexpression of MANF K96A and MANF R155A do not affect ER stress-induced IRE1α oligomerization in IRE1α-3F6HGFP-inducible cell line. In (A) and (B) ER stress was induced by 5 μg/mL tunicamycin (TM) for 4 h. The numbers of IRE1α-GFP foci to total cell count are indicated. One-way ANOVA, Dunnett's post hoc test, n = 3; **p < 0.01, ****p < 0.0001.

(C) Labeled IRE1α LD is not interacting with MANF K96A (0–4.6 μM), while its affinity to MANF K128AC130S (0–4.6 μM) is the same as to wtMANF (0–4.6 μM).

(D) Interaction of IRE1α LD (0–6.56 μM) with labeled IRE1α LD is not affected in the presence of 1 μM of MANF and is abolished in the presence 5 μM of MANF.

(E) Interaction of IRE1α LD (0–6.56 μM) with labeled IRE1α LD is not affected by 1 or 5 μM MANF K96A. In (C)–(E) the labeled targets were used at 20 nM. MST binding curves, showing mean ΔFnorm values from n = 3–4 repeats per binding pair ± SEM. Kd values ± error estimations are indicated.

A

time 30' 30' 30' 60' 60' 60' 240' 240' 240'
TM − + + − + + − + +
MANF − − + − − + − − +

pSer724 IRE1α — 130 kDa

α-tubulin — 50 kDa

B *sXbp1*

C *Txnip*

D

DA
DA,TG+
DA,TG+, MANF+
DA,TG+,MANF K96A+

E SCG neurons

F SCG neurons

G DA neurons

H DA neurons

I MANF/MANF mutants - IRE1α LD

wtMANF Kd=131.9±36.3 nM
MANF R133E Kd=140.2±42.3 nM
MANF E153A Kd=199.8±84.6 nM

J MANF/MANF mutants - BiP

MANF K96A Kd=123.4±50.4 nM
MANF K128AC130S Kd=244.9±104.3 nM
wtMANF Kd=473.3±193 nM
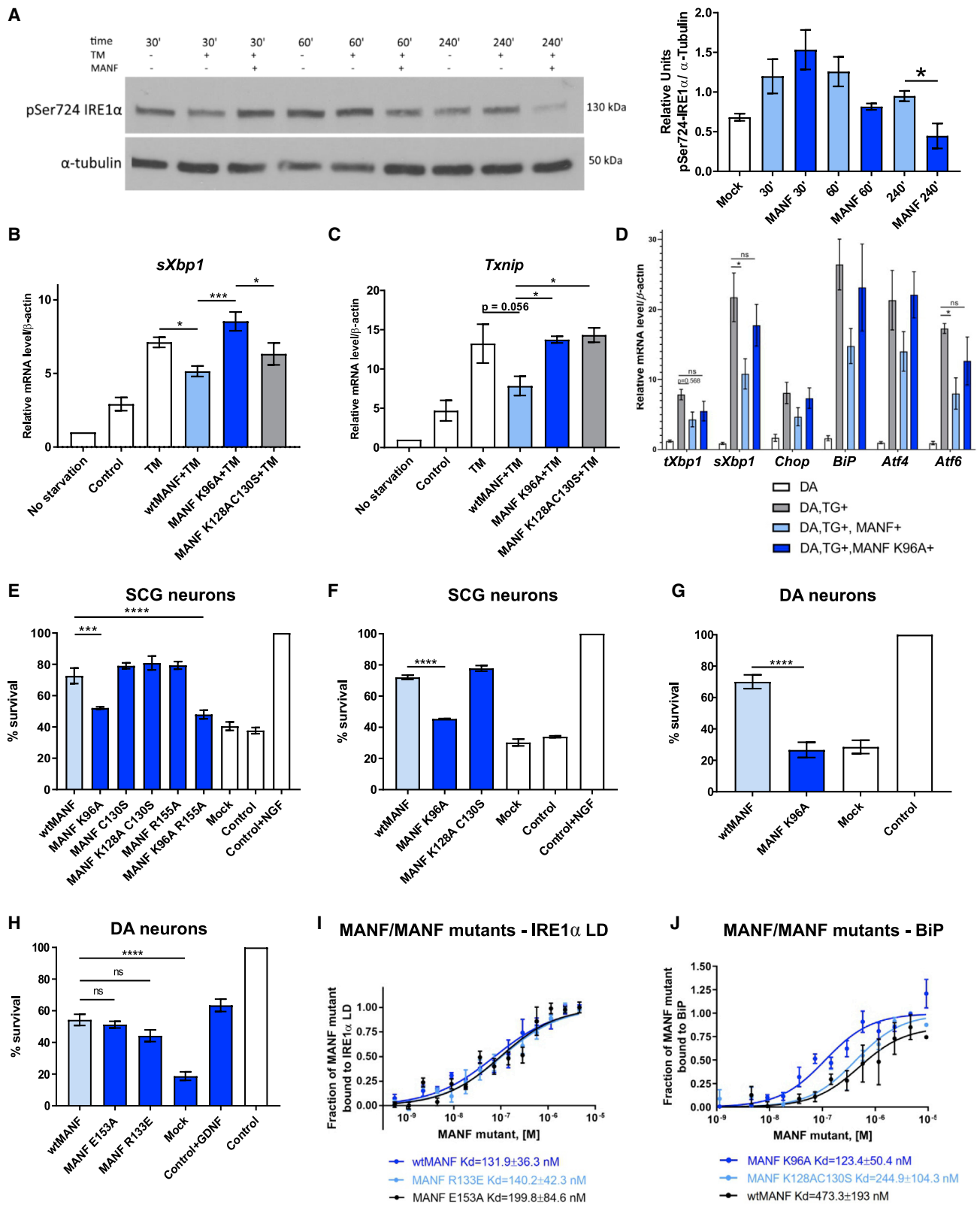
(legend on next page)

MANF-IRE1α interaction is crucial for the protection of mouse sympathetic and dopamine neurons from ER stress-induced death

To test whether the MANF mutations abolishing IRE1α binding affect the pro-survival activity of MANF, we microinjected the respective expression plasmids or mutant proteins into mouse SCG neurons, which were then induced to die with TM. We found that the K96A mutation abolished pro-survival activity of MANF, and that the double mutant K96A R155A was biologically inactive (Figure 6E). Surprisingly, the R155A mutation and both cysteine loop mutations C130S and K128AC130S did not affect pro-survival activity of MANF.

We then tested MANF K96A, deficient for IRE1α LD binding, and MANF K128AC130S, binding IRE1α LD, by microinjecting the respective proteins into mouse SCG neurons that were then treated with TM. We found that MANF K96A was not able to protect SCG neurons from TM-induced death, while MANF K128AC130S exhibited a similar pro-survival activity as wtMANF (Figure 6F).

We found that K96A mutation also completely abolished the cytoprotective effect of MANF against TG-induced death in DA neurons (Figure 6G), confirming that MANF-IRE1α LD interaction is crucial for pro-survival activity of MANF also in DA neurons.

MANF-BiP interaction is dispensable for rescuing mouse sympathetic and dopamine neurons from ER stress-induced death

Since MANF was earlier shown to regulate protein-folding homeostasis through interaction with BiP,[16,35] we investigated whether the deficiency in BiP binding affects pro-survival properties of MANF in DA neurons upon ER stress. We found that MANF E153A and MANF R133E, deficient in BiP binding,[16,35] protected DA neurons from TG-induced ER stress (Figure 6H).

To investigate whether BiP could abolish the MANF-IRE1α LD interaction by sequestering MANF, we tested MANF E153A and MANF R133E for binding to IRE1α LD and found that MANF E153A and MANF R133E were binding IRE1α LD with similar affinities as wtMANF, confirming that binding sites for BiP and IRE1α LD in MANF are different (Figure 6I). In addition, we tested whether BiP affects the binding of MANF E153A and MANF R133E to IRE1α LD and found that similarly to wtMANF 50 nM BiP abolishes the interaction of BiP binding-deficient MANF mutants with IRE1α LD (Figure S6F). These results demonstrate that the BiP-MANF interaction does not affect BiP competition with MANF for IRE1α LD binding. To establish whether the abolishment of pro-survival effects for IRE1α binding-deficient MANF K96A could result from changes in its ability to bind BiP we tested if it interacted with BiP using MST. We found that MANF K96A and MANF K128AC130S interacted with BiP similarly to wtMANF (Figure 6J).

MANF-IRE1α LD interaction is needed for neuroprotective effects of MANF in vivo

To test whether MANF-IRE1α interaction is important for the neurorestorative activity of MANF in vivo, we went on to investigate the effects of wtMANF and MANF K96A proteins in a rat 6-hydroxydopamine (6-OHDA) model of PD, as described previously.[7,45]

The animals were injected with wtMANF, MANF K96A, or vehicle intrastriatally 2 weeks after 6-OHDA lesioning (Figure 7A). Single intrastriatal wtMANF injection reduced amphetamine-induced ipsilateral turning behavior compared with vehicle-treated rats, with maximal effect at 12 weeks after lesioning (Figure 7B). MANF K96A injection had no effect on rotational behavior, confirming that MANF-IRE1α interaction is crucial for restoring motor imbalance in the animal model of PD.

The number of TH-positive cells in substantia nigra pars compacta (SNpc) was measured as a percentage of control (intact side) in the rostral, central, and caudal parts of the SNpc. We have shown that the injection of wtMANF protected TH-positive cells in the caudal part of the SNpc and tended to increase the number of TH-positive cells in other parts of the SNpc (Figures 7C–7D). MANF K96A-injected animals had a similar number of TH-positive cells as the animals from the vehicle-injected group. Well in line with the earlier observations, neither wtMANF[7] nor MANF K96A affected TH-positive fiber density and DAT-positive fiber density in the striatum (Figures S6G and S6H). Our results demonstrate that MANF-IRE1α interaction is crucial for neurorestorative activity of MANF in the animal model of PD in vivo.

Figure 6. MANF decreases phosphorylation of IRE1α. MANF-IRE1α interaction is crucial for the survival of mouse sympathetic and dopamine neurons under ER stress

(A) Representative image and quantification of pSer724 IRE1α in IRE1α-HA-MEFs treated for 4 h with tunicamycin (TM) 1 μg/μL, followed by 30, 60, and 240 min of treatment with human MANF (50 nM). Mean ± SEM; n = 3; Student's t test; *p < 0.05.

(B and C) (B) sXbp1 and (C) Txnip mRNA levels in MEFs treated for 4 h with TM 100 ng/mL, followed by 20 h of treatment with 150 nM MANF, MANF K96A, or MANF K128AC130S, as measured using qPCR. Mean ± SEM; n = 4 and n = 3, respectively.

(D) MANF and not MANF K96A added to the cultured dopamine (DA) neurons decreases the expression levels of UPR transcripts upon 24 h thapsigargin (TG)-induced ER stress as measured using qPCR (normalization to β-actin). Mean ± SEM; n = 4.

(E) Microinjections of MANF K96A or MANF K96AR155A plasmids to SCG neurons do not rescue them from TM-induced cell death compared with mock-injected with empty vector or uninjected. Mean ± SEM; n = 3.

(F) Microinjection of MANF K96A protein to SCG neurons does not rescue them from TM-induced cell death compared with mock-injected with Dextran, Texas red, or uninjected neurons. Mean ± SEM; n = 4.

(G) MANF K96A is not protecting DA neurons from ER stress induced by treatment with TG.

(H) BiP binding-deficient MANF R133E and MANF E153A are protecting DA neurons from ER stress induced with TG similarly to wtMANF. In (B)–(H) one-way ANOVA, Tukey's post hoc test. *p < 0.05, **p < 0.01,***p < 0.001, ****p < 0.0001. In (C), (F), and (G) wtMANF or MANF mutants were added to the cultures at 100 ng/mL together with 200 nM TG. Mean ± SEM; n = 4.

(I) Deficient for BiP binding, MANF E153A and MANF R133E (0–4.6 μM) interact with labeled IRE1α LD similarly to wtMANF.

(J) MANF K96A and MANF K128AC130S (0–9.3 μM) interact with labeled BiP similarly to wtMANF. In (I) and (J) the labeled targets were used at 20 nM. MST binding curves, showing mean fraction bond values from n = 3–4 repeats per binding pair ± SEM. K_d values ± error estimations are indicated.
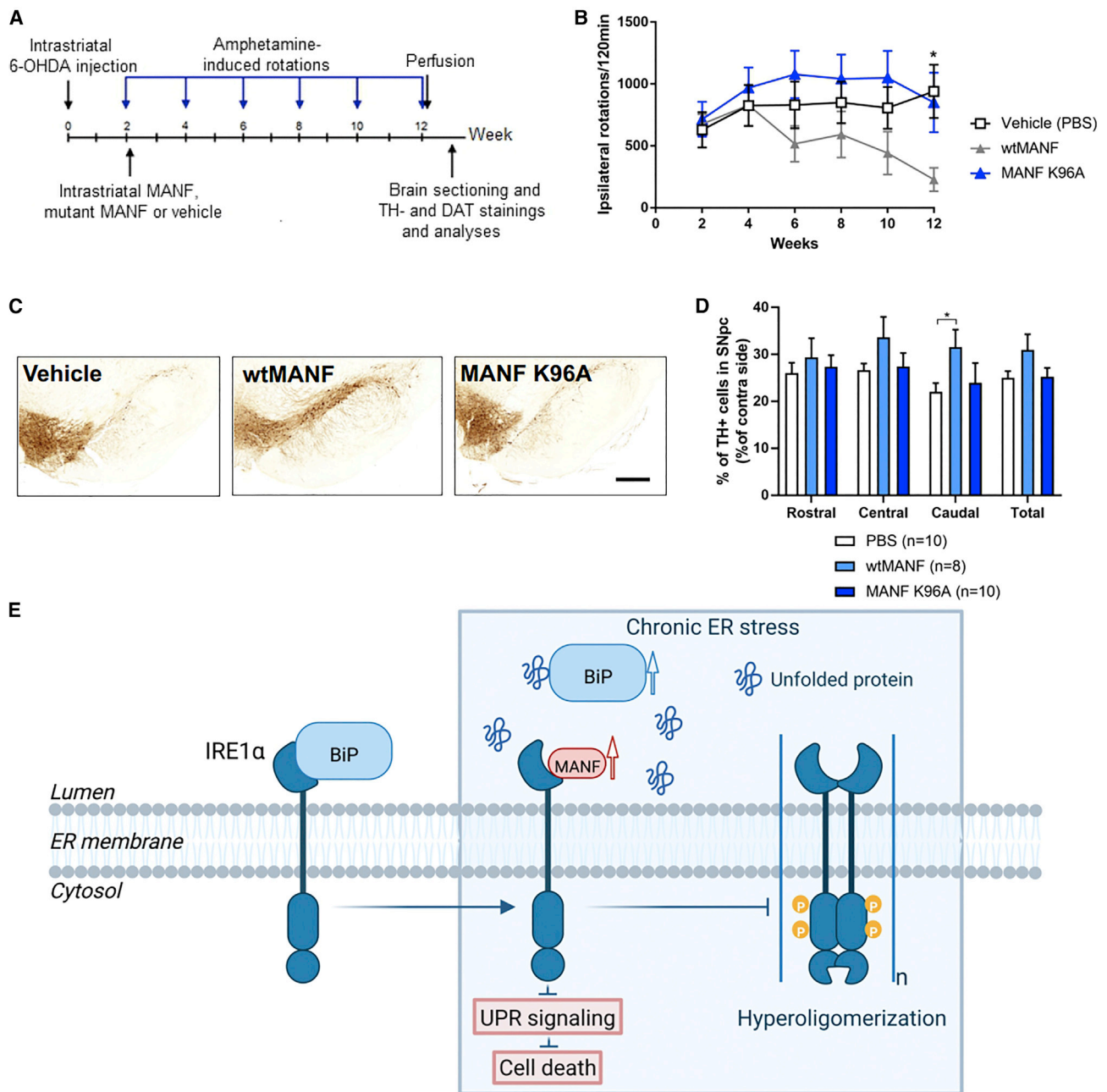
Figure 7. MANF K96A does not affect rotational behavior and number of TH-positive neurons in a rat 6-OHDA model of Parkinson's disease

(A) Experimental paradigm for the study of testing of MANF K96A activity in animal PD model.

(B) Amphetamine-induced rotations. Vehicle-treated rats show robust turning behavior. Single intrastriatal wtMANF injection reduces turning behavior compared with vehicle-treated rats. p = 0.0166.

(C) Representative images of substantia nigra pars compacta (SNpc) (lesioned side) from the groups injected with vehicle (PBS), wtMANF, or deficient for IRE1α binding MANF K96A. Scale bar, 500 μm.

(D) Quantification of the percent of TH-positive cells in rostral, central, and caudal parts of SNpc. Two-way ANOVA; *$p < 0.05$.

(E) Putative mechanism of MANF signaling through IRE1α. Upon ER stress MANF and BiP levels are increasing, and when BiP dissociates from IRE1α LD or its oligomerization site to bind misfolded proteins, progressively accumulating in the ER lumen, MANF can directly bind to IRE1α LD. This binding is preventing IRE1α hyperoligomerization, decreasing IRE1α phosphorylation, and downregulating downstream targets of IRE1α LD, resulting in neuroprotective and neuro-restorative effect both *in vitro* and *in vivo*.

DISCUSSION

IRE1α is the most evolutionary conserved and well-studied UPR sensor. However, the mechanisms of its activation and regulation remain poorly understood and involve not only BiP but also other proteins.[21,27,28]

Here, we characterize MANF as a regulator-inhibitor of IRE1α activation under ER stress. To date, MANF has been shown to alleviate ER stress *in vitro* and *in vivo* through unclear mechanisms.[8,9,11–15,46]

The data we present here give insights into the MANF mechanism of action in the ER. Since the MANF binding site in IRE1α LD overlaps that of BiP, MANF can bind to IRE1α only if BiP is dissociated from IRE1α LD or its oligomerization site. Thus, MANF is acting only in highly stressed and not in naive cells. Therefore, therapeutically used MANF is unlikely to cause serious negative side effects in healthy cells.

According to the affinities to UPR sensors, BiP dissociates first from IRE1α and thus MANF binds first to IRE1α and only then to PERK and ATF6. MANF-IRE1α binding may therefore be physiologically more significant than MANF binding to other UPR sensors. In competition experiments the priority of BiP over MANF in IRE1α binding can be explained by an allosteric conformational change in IRE1α LD induced by BiP binding and preventing MANF binding to IRE1α LD in the presence of BiP. Alternatively, since BiP is more than four times larger than MANF, its binding site in IRE1α LD may be correspondingly larger, so its binding may block MANF binding more than *vice versa*. The difference in curve slopes for MANF and BiP binding to IRE1α may occur due to the binding of BiP and MANF to different oligomeric forms of IRE1α. Since BiP likely interacts with dimeric/oligomeric IRE1α and in equilibrium the ratio of IRE1α forms is shifted to more oligomeric, the binding curve is steeper than that of MANF, not able to interact with IRE1α oligomers, and has a rather limited number of monomeric interactors. BiP priority over MANF could be also explained by the presence of several BiP binding sites in IRE1α LD.

In support of crosstalk between endogenous MANF and IRE1α, we found that knockdown of MANF in HEK293 cells induced upregulation of IRE1α. *In vivo* depletion of MANF is known to induce activation of the IRE1α pathway and upregulation of UPR genes downstream of IRE1α,[8,15] whereas upregulation of IRE1α due to a decrease in MANF level has not been reported previously. Spliced XBP1 is known to induce MANF expression,[12,47] thus upregulation of IRE1α is likely an attempt to compensate for MANF depletion in cells. We demonstrated that endogenous MANF and IRE1α reside in a protein complex. However, whether the observed MANF-IRE1α interaction in cells is direct or mediated by other molecules is unclear. IRE1α was detected in the MANF co-IP complex in naive cells and under ER stress. Chronic TG-induced ER stress upregulated IRE1α and also increased its level in the MANF co-IP complex, possibly indicating the presence of the oligomeric form of IRE1α in this complex. Although chronic TM treatment upregulated IRE1α, differently from TG treatment it did not affect the level of IRE1α in the MANF co-IP complex. In line with our MST data, TG-induced Ca²⁺ depletion from the ER could facilitate MANF-IRE1α interaction in cells, which explains the elevated levels of IRE1α in the MANF co-IP complex after TG treatment.

In addition to IRE1α, BiP was also present in the MANF protein complex. Interaction dynamics between endogenous MANF, IRE1α, and BiP, and the question of whether BiP prevents the interaction of endogenous MANF and IRE1α remains to be studied further.

Using computational modeling, we identified the IRE1α binding site in MANF and biologically inactive *in vitro* and *in vivo* MANF K96A mutant. K96 is located in the linker region in the C-terminal domain of MANF, suggesting that the residues crucial for interaction are located in the linker region (K96-T105) in C-MANF, which is in line with our MST and BiFC data. The additional docking calculations using the full-length structures of MANF and IRE1α LD confirmed that the linker region in the C-MANF is important for MANF-IRE1α LD interaction. The results of the further docking study of the binding between full-length MANF mutants (K96A, R155A) and IRE1α LD showed that the intrinsically disordered region of IRE1α LD (V308-N357) and the oligomerization site (region 4) can be crucial for MANF binding. The conformational changes in this disordered region are known to be responsible for the transition of IRE1α LD from a "closed" to an "open" conformation, preceding IRE1α LD activation.[21] Thus, MANF could inhibit IRE1α activation through blocking of the conformational changes in the unstructured region of IRE1α LD upon ER stress.

Generated IRE1α LD mutants, except for the dimerization site mutant, were deficient for MANF binding. Since other regions are located on the opposite side to the surface of the dimerization site of IRE1α LD protein, they could represent a single MANF binding site. The binding of MANF near the oligomerization site supports our main findings on MANF inhibition of IRE1α-oligomerization in cells and using MST. IRE1α LD binding-deficient MANF K96A does not abolish IRE1α-IRE1α interaction in MST, confirming that MANF affects IRE1α oligomerization through direct binding. MANF binding sites in IRE1α (regions 3 and 4) are overlapping with the sites suggested to be involved in BiP interaction with IRE1α LD.[24,48] Further computational and structural studies are of great importance. It has been shown previously that, during ER stress progression, MANF expression levels increase[11] and the fraction of IRE1α-bound BiP decreases.[3] This could facilitate MANF binding to IRE1α, which in turn regulates the intensity of the IRE1α-mediated UPR response by decreasing or preventing IRE1α hyperoligomerization, decreasing IRE1α phosphorylation, splicing of XBP1, and cell death.

In MEFs, MANF decreases IRE1α phosphorylation at Ser724 most likely by stabilizing the monomeric or dimeric conformation of IRE1α, preventing IRE1α oligomerization and autophosphorylation. Alternatively, MANF binding can stabilize IRE1α in conformation favoring the recruitment of soluble kinases or phosphatases affecting IRE1α phosphorylation at Ser724 and possibly at other sites. We showed that, upon chronic TG-induced ER stress, the amount of IRE1α in the MANF protein complex profoundly increases, which is accompanied by a decrease in phospho-IRE1α, suggesting that, upon chronic ER stress induced by calcium depletion, increase in MANF-IRE1α complex formation correlates with inhibited activity of IRE1α.

During adaptive UPR IRE1α activation is protective, mainly through sXBP1.[47,49,50] However, in some cases, a high level of

sXBP1 resulted in the release of pro-inflammatory extracellular vesicles upon lipotoxic ER stress in hepatocytes[51] or induction of acetyltransferase P300, impairing insulin signaling.[52] sXBP1 also has unexpected targets, about 40% of them are unrelated to sXBP1 function in ER and include many genes involved in neuro- and myodegenerative diseases, differentiation, and DNA damage and repair.[53] IRE1α was recently demonstrated to have two endoribonuclease modalities correlating with the IRE1α phospho-oligomeric state.[54] Inhibition of one of these modalities (requiring phospho-oligomers and mediating RIDDLE) by MANF may result in its pro-survival activity. We found that extracellularly applied MANF downregulates sXbp1 level in MEFs upon ER stress. In DA neurons, MANF downregulated sXbp1 and Atf6 levels, and tended to decrease tXbp1 level, indicating that the pro-survival effect can occur not only through sXbp1 downregulation but also through other targets of IRE1α. These effects were not observed when IRE1α binding-deficient MANF K96A was used. Likely the pro-survival action of MANF is elicited not only through the downregulation of sXbp1 but also through the prevention of activation of pro-apoptotic pathways known to be triggered by hyperactivated IRE1α. Upon chronic severe unresolved ER stress, hyperactivated and hyperoligomerized IRE1α is known to trigger JNK/MAPK-mediated apoptosis and transcription of pro-inflammatory genes.[55,56] IRE1α hyperoligomerization has been also shown to upregulate thioredoxin-interacting protein (TNXIP), activating the NLRP3 inflammasome, and promoting apoptosis.[57] We demonstrated that MANF tended to decrease the level of Txnip in MEFs, while IRE1α-binding-deficient MANF K96A and also MANF K128AC130S did not affect Txnip level. The pro-survival action of MANF through the prevention of IRE1α hyperoligomerization can be also due to the inhibition of the canonical NF-κB pathway shown to be triggered by IRE1α activation through the degradation of IκB by IRE1α upon ER stress.[30,58–60]

Using earlier described BiP-binding-deficient MANF mutants,[35] we demonstrated that MANF-IRE1α binding and not MANF-BiP binding is crucial for the pro-survival effect of MANF both in SCG and DA neurons. Based on our findings, we propose that MANF may represent a "second wave" of UPR regulation, following BiP dissociation from IRE1α (Figure 7E). MANF via its linker region in the C-terminal domain binds to IRE1α close to its oligomerization site and prevents IRE1α oligomerization and hyperactivation upon chronic ER stress. This promotes cell survival through regulation of IRE1α phosphorylation, reduction of sXbp1, and prevention of triggering of IRE1α hyperactivation-induced pro-apoptotic mechanisms, such as Txnip upregulation. Alternatively, MANF binding can occur after the dissociation of BiP from one of its several potential binding sites in IRE1α LD, overlapping with the IRE1α oligomerization site, but BiP binding to other binding sites in IRE1α LD can still occur. In this case, the presence of MANF in complex with IRE1α would not necessarily correlate with BiP dissociation from IRE1α; however, it can correlate with IRE1α activity.

Importantly, we have also demonstrated that MANF-IRE1α interaction is crucial for the neuroprotective activity of MANF in animal model of PD. This brings to light perspectives and strategies in the treatment of PD and other neurodegenerative and UPR-associated diseases, such as diabetes, through attenuation of IRE1α signaling. In line with this, a specific inhibitor of IRE1α signaling KIRA8 was shown to have anti-diabetic effects.[57,61] Another attenuator of IRE1α signaling, the c-Abl inhibitor Imatinib (Gleevec), was shown to restore cognitive function and have a neuroprotective potential in the LPS-induced murine inflammation model.[62] MANF action resembles that of the attenuators of IRE1α signaling, but MANF interacts with all three UPR sensors and therefore could be more potent as a neuroprotective and anti-diabetic agent. Future in vitro screening of small-molecule compounds mimicking MANF action on IRE1α and other UPR sensors can lead to the development of drugs for the treatment of PD, diabetes, and other UPR-associated diseases.

Limitations of the study

We have not managed to crystallize MANF-IRE1α LD complex, likely because MANF binding could occur through an unstructured region of IRE1α similarly to that of BiP. Therefore, an extensive computational modeling work has been performed. A limited characterization of MANF and BiP competition in cells is provided, and the NMR or SAXS demonstration of possible conformational change in IRE1α LD upon BiP dissociation, facilitating MANF binding to IRE1α LD is missing. We show that the targets of IRE1α regulated by MANF could be cell type and ER stress conditions specific, therefore a thorough correlation between the stage of ER stress and downstream signaling in different cells should be addressed. One more limitation is the absence of extensive characterization of IRE1α LD mutants deficient for MANF binding. In a follow-up study, these mutations should be introduced into full-length IRE1α and their activation/phosphorylation and ability to perform splicing of XBP1 and RIDD/RIDDLE, as well as activated downstream signaling, should be investigated.

STAR★METHODS

Detailed methods are provided in the online version of this paper and include the following:

- KEY RESOURCES TABLE
- RESOURCE AVAILABILITY
  - Lead contact
  - Materials availability
  - Data and code availability
- EXPERIMENTAL MODEL AND SUBJECT DETAILS
  - Experimental animals
  - Primary cell cultures
  - Cell lines
- METHOD DETAILS
  - Reagents and proteins
  - Microscale thermophoresis (MST)
  - Binding assay on nickel-coated plates
  - Analysis of purity and glycosylation of LDs of UPR sensors
  - Size exclusion chromatography
  - Protein – protein docking
  - Homology modelling and optimization of the full-length structure of IRE1α LD

- ○ Knockdown of MANF using siRNA
- ○ Crosslinking and co-immunoprecipitation (co-IP)
- ○ Analysis of IRE1α phosphorylation
- ○ Generation of MANF mutant plasmids and recombinant proteins
- ○ Generation of IRE1α LD mutant plasmids and recombinant proteins
- ○ Duolink proximity ligation assay (PLA)
- ○ Plasmids for bimolecular fluorescence complementation assay (BiFC)
- ○ BiFC and immunocytochemistry
- ○ IRE1α oligomerization assay
- ○ Western blot analysis
- ○ Real-time quantitative PCR (RT-qPCR)
- ○ SCG neuronal culture microinjections
- ○ Immunocytochemistry
- ○ MANF treatment in primary cultures of midbrain dopamine neurons
- ○ RNA isolation, reverse transcription and quantitative RT-qPCR in dopamine neurons
- ○ Testing MANF mutant in *in vivo* 6-OHDA model. 6-OHDA lesioning
- ○ Intrastriatal administration of compounds
- ○ Immunohistochemistry
- ○ Morphological analyses
- ● QUANTIFICATION AND STATISTICAL ANALYSIS

AUTHOR CONTRIBUTIONS

Conceptualization, V.K. and M.S.; methodology, V.K., L.I., and P.L.; investigation, V.K., L.-Y.Y., L.I., O.S., A.E., E.-P.K., S.S., and P.L.; *in vivo* investigation, M.H.V. and J.N.; formal analysis, V.K., L.-Y.Y., L.I., and P.L.; *in vivo* investigation, J.N.; writing – original draft, V.K., L.I., P.L., and M.S.; writing – review & editing, V.K., L.I., P.L., and M.S.; project administration and funding acquisition, M.S.; resources, U.T. and M.U.; supervision, V.K., J.T.H., M.H.V., M.K., and M.S.

DECLARATION OF INTERESTS

The authors declare no competing interests. M.S., P.L., and M.H.V. are the inventors in the MANF-related patent owned by Herantis Pharma Plc. M.S. is also a shareholder in Herantis Pharma Plc.

REFERENCES

1. Walter, P., and Ron, D. (2011). The unfolded protein response: from stress pathway to homeostatic regulation. Science *334*, 1081–1086. https://doi.org/10.1126/science.1209038.

2. Cox, J.S., Shamu, C.E., and Walter, P. (1993). Transcriptional induction of genes encoding endoplasmic reticulum resident proteins requires a transmembrane protein kinase. Cell *73*, 1197–1206. https://doi.org/10.1016/0092-8674(93)90648-A.

3. Bertolotti, A., Zhang, Y., Hendershot, L.M., Harding, H.P., and Ron, D. (2000). Dynamic interaction of BiP and ER stress transducers in the unfolded-protein response. Nat. Cell Biol. *2*, 326–332. https://doi.org/10.1038/35014014.

4. Prischi, F., Nowak, P.R., Carrara, M., and Ali, M.M.U. (2014). Phosphoregulation of Ire1 RNase splicing activity. Nat. Commun. *5*, 3554. https://doi.org/10.1038/ncomms4554.

5. Petrova, P.S., Raibekas, A., Pevsner, J., Vigo, N., Anafi, M., Moore, M.K., Peaire, A.E., Shridhar, V., Smith, D.I., Kelly, J., et al. (2003). MANF: a new mesencephalic, astrocyte-derived neurotrophic factor with selectivity for dopaminergic neurons. J. Mol. Neurosci. *20*, 173–188. https://doi.org/10.1385/JMN:20:2:173.

6. Lindholm, P., and Saarma, M. (2022). Cerebral dopamine neurotrophic factor protects and repairs dopamine neurons by novel mechanism. Mol. Psychiatry *27*, 1310–1321. https://doi.org/10.1038/s41380-021-01394-6.

7. Voutilainen, M.H., Bäck, S., Pörsti, E., Toppinen, L., Lindgren, L., Lindholm, P., Peränen, J., Saarma, M., and Tuominen, R.K. (2009). Mesencephalic astrocyte-derived neurotrophic factor is neurorestorative in rat model of Parkinson's disease. J. Neurosci. *29*, 9651–9659. https://doi.org/10.1523/JNEUROSCI.0833-09.2009.

8. Lindahl, M., Danilova, T., Palm, E., Lindholm, P., Võikar, V., Hakonen, E., Ustinov, J., Andressoo, J.O., Harvey, B.K., Otonkoski, T., et al. (2014). MANF is indispensable for the proliferation and survival of pancreatic β cells. Cell Rep. *7*, 366–375. https://doi.org/10.1016/j.celrep.2014.03.023.

9. Danilova, T., Belevich, I., Li, H., Palm, E., Jokitalo, E., Otonkoski, T., and Lindahl, M. (2019). MANF is required for the postnatal expansion and maintenance of pancreatic β-cell mass in mice. Diabetes *68*, 66–80. https://doi.org/10.2337/db17-1149.

10. Sousa-Victor, P., Neves, J., Cedron-Craft, W., Ventura, P.B., Liao, C.Y., Riley, R.R., Soifer, I., van Bruggen, N., Kolumam, G.A., Villeda, S.A., et al. (2019). MANF regulates metabolic and immune homeostasis in ageing and protects against liver damage. Nat. Metab. *1*, 276–290. https://doi.org/10.1038/s42255-018-0023-6.

11. Apostolou, A., Shen, Y., Liang, Y., Luo, J., and Fang, S. (2008). Armet, a UPR-upregulated protein, inhibits cell proliferation and ER stress-induced cell death. Exp. Cell Res. *314*, 2454–2467. https://doi.org/10.1016/j.yexcr.2008.05.001.

12. Mizobuchi, N., Hoseki, J., Kubota, H., Toyokuni, S., Nozaki, J.I., Naitoh, M., Koizumi, A., and Nagata, K. (2007). ARMET is a soluble ER protein induced by the unfolded protein response via ERSE-II element. Cell Struct. Funct. *32*, 41–50. https://doi.org/10.1247/csf.07001.

13. Tadimalla, A., Belmont, P.J., Thuerauf, D.J., Glassy, M.S., Martindale, J.J., Gude, N., Sussman, M.A., and Glembotski, C.C. (2008). Mesencephalic astrocyte-derived neurotrophic factor is an ischemia-inducible secreted endoplasmic reticulum stress response protein in the heart. Circ. Res. *103*, 1249–1258. https://doi.org/10.1161/CIRCRESAHA.108.180679.

14. Hellman, M., Arumäe, U., Yu, L.Y., Lindholm, P., Peränen, J., Saarma, M., and Permi, P. (2011). Mesencephalic astrocyte-derived neurotrophic factor (MANF) has a unique mechanism to rescue apoptotic neurons. J. Biol. Chem. *286*, 2675–2680. https://doi.org/10.1074/jbc.M110.146738.

15. Pakarinen, E., Danilova, T., Võikar, V., Chmielarz, P., Piepponen, P., Airavaara, M., Saarma, M., and Lindahl, M. (2020). MANF ablation causes prolonged activation of the UPR without neurodegeneration in the mouse midbrain dopamine system. eNeuro 7, ENEURO.0477, ENEURO19.2019. https://doi.org/10.1523/ENEURO.0477-19.2019.

16. Eesmaa, A., Yu, L.-Y., Göös, H., Nõges, K., Kovaleva, V., Hellman, M., Zimmermann, R., Jung, M., Permi, P., Varjosalo, M., et al. (2021). The cytoprotective protein MANF promotes neuronal survival independently from its role as a GRP78 cofactor. J. Biol. Chem. 296, 100295. https://doi.org/10.1016/j.jbc.2021.100295.

17. Hartman, J.H., Richie, C.T., Gordon, K.L., Mello, D.F., Castillo, P., Zhu, A., Wang, Y., Hoffer, B.J., Sherwood, D.R., Meyer, J.N., and Harvey, B.K. (2019). MANF deletion abrogates early larval Caenorhabditis elegans stress response to tunicamycin and Pseudomonas aeruginosa. Eur. J. Cell Biol. 98, 151043. https://doi.org/10.1016/j.ejcb.2019.05.002.

18. Danilova, T., Galli, E., Pakarinen, E., Palm, E., Lindholm, P., Saarma, M., and Lindahl, M. (2019). Mesencephalic astrocyte-derived neurotrophic factor (MANF) is highly expressed in mouse tissues with metabolic function. Front. Endocrinol. 10, 765. https://doi.org/10.3389/fendo.2019.00765.

19. Bommiasamy, H., and Popko, B. (2011). Animal models in the study of the unfolded protein response. In Methods in Enzymology (Academic Press Inc.), pp. 91–109. https://doi.org/10.1016/B978-0-12-385928-0.00006-7.

20. Hetz, C. (2012). The unfolded protein response: controlling cell fate decisions under ER stress and beyond. Nat. Rev. Mol. Cell Biol. 13, 89–102. https://doi.org/10.1038/nrm3270.

21. Karagöz, G.E., Acosta-Alvear, D., Nguyen, H.T., Lee, C.P., Chu, F., and Walter, P. (2017). An unfolded protein-induced conformational switch activates mammalian IRE1. Elife 6, e30700. https://doi.org/10.7554/eLife.30700.

22. Amin-Wetzel, N., Saunders, R.A., Kamphuis, M.J., Rato, C., Preissler, S., Harding, H.P., and Ron, D. (2017). A J-protein Co-chaperone recruits BiP to monomerize IRE1 and repress the unfolded protein response. Cell 171, 1625–1637.e13. https://doi.org/10.1016/j.cell.2017.10.040.

23. Preissler, S., and Ron, D. (2019). Early events in the endoplasmic reticulum unfolded protein response. Cold Spring Harb. Perspect. Biol. 11, a033894. https://doi.org/10.1101/cshperspect.a033894.

24. Carrara, M., Prischi, F., Nowak, P.R., Kopp, M.C., and Ali, M.M. (2015). Noncanonical binding of BiP ATPase domain to Ire1 and Perk is dissociated by unfolded protein CH1 to initiate ER stress signaling. Elife 4, e03522. https://doi.org/10.7554/eLife.03522.

25. Kopp, M.C., Nowak, P.R., Larburu, N., Adams, C.J., and Ali, M.M. (2018). In vitro FRET analysis of IRE1 and BiP association and dissociation upon endoplasmic reticulum stress. Elife 7, e30257. https://doi.org/10.7554/eLife.30257.

26. Belyy, V., Zuazo-Gaztelu, I., Alamban, A., Ashkenazi, A., and Walter, P. (2022). Endoplasmic reticulum stress activates human IRE1α through reversible assembly of inactive dimers into small oligomers. Elife 11, e74342. https://doi.org/10.7554/eLife.74342.

27. Sepulveda, D., Rojas-Rivera, D., Rodríguez, D.A., Groenendyk, J., Köhler, A., Lebeaupin, C., Ito, S., Urra, H., Carreras-Sureda, A., Hazari, Y., et al. (2018). Interactome screening identifies the ER luminal chaperone Hsp47 as a regulator of the unfolded protein response transducer IRE1α. Mol. Cell 69, 238–252.e7. https://doi.org/10.1016/j.molcel.2017.12.028.

28. Eletto, D., Eletto, D., Dersh, D., Gidalevitz, T., and Argon, Y. (2014). Protein disulfide isomerase A6 controls the decay of IRE1α signaling via disulfide-dependent association. Mol. Cell 53, 562–576. https://doi.org/10.1016/j.molcel.2014.01.004.

29. Mätlik, K., Yu, L.y., Eesmaa, A., Hellman, M., Lindholm, P., Peränen, J., Galli, E., Anttila, J., Saarma, M., Permi, P., et al. (2015). Role of two sequence motifs of mesencephalic astrocyte-derived neurotrophic factor in its survival-promoting activity. Cell Death Dis. 6, e2032. https://doi.org/10.1038/cddis.2015.371.

30. Hakonen, E., Chandra, V., Fogarty, C.L., Yu, N.Y.L., Ustinov, J., Katayama, S., Galli, E., Danilova, T., Lindholm, P., Vartiainen, A., et al. (2018). MANF protects human pancreatic beta cells against stress-induced cell death. Diabetologia 61, 2202–2214. https://doi.org/10.1007/s00125-018-4687-y.

31. Cunha, D.A., Cito, M., Grieco, F.A., Cosentino, C., Danilova, T., Ladrière, L., Lindahl, M., Domanskyi, A., Bugliani, M., Marchetti, P., et al. (2017). Pancreatic β-cell protection from inflammatory stress by the endoplasmic reticulum proteins thrombospondin 1 and mesencephalic astrocyte-derived neutrotrophic factor (MANF). J. Biol. Chem. 292, 14977–14988. https://doi.org/10.1074/jbc.M116.769877.

32. Yagi, T., Asada, R., Kanekura, K., Eesmaa, A., Lindahl, M., Saarma, M., and Urano, F. (2020). Neuroplastin modulates anti-inflammatory effects of MANF. iScience 23, 101810. https://doi.org/10.1016/j.isci.2020.101810.

33. Glembotski, C.C., Thuerauf, D.J., Huang, C., Vekich, J.A., Gottlieb, R.A., and Doroudgar, S. (2012). Mesencephalic astrocyte-derived neurotrophic factor protects the heart from ischemic damage and is selectively secreted upon sarco/endoplasmic reticulum calcium depletion. J. Biol. Chem. 287, 25893–25904. https://doi.org/10.1074/jbc.M112.356345.

34. Bell, P.A., Dennis, E.P., Hartley, C.L., Jackson, R.M., Porter, A., Boot-Handford, R.P., Pirog, K.A., and Briggs, M.D. (2019). Mesencephalic astrocyte-derived neurotropic factor is an important factor in chondrocyte ER homeostasis. Cell Stress Chaperones 24, 159–173. https://doi.org/10.1007/s12192-018-0953-7.

35. Yan, Y., Rato, C., Rohland, L., Preissler, S., and Ron, D. (2019). MANF antagonizes nucleotide exchange by the endoplasmic reticulum chaperone BiP. Nat. Commun. 10, 541. https://doi.org/10.1038/s41467-019-08450-4.

36. Haze, K., Yoshida, H., Yanagi, H., Yura, T., and Mori, K. (1999). Mammalian transcription factor ATF6 is synthesized as a transmembrane protein and activated by proteolysis in response to endoplasmic reticulum stress. Mol. Biol. Cell 10, 3787–3799.

37. Zampese, E., and Pizzo, P. (2012). Intracellular organelles in the saga of Ca 2+ homeostasis: different molecules for different purposes? Cell. Mol. Life Sci. 69, 1077–1104. https://doi.org/10.1007/s00018-011-0845-9.

38. Chuang, G.Y., Kozakov, D., Brenke, R., Comeau, S.R., and Vajda, S. (2008). DARS (Decoys as the Reference State) potentials for protein-protein docking. Biophys. J. 95, 4217–4227. https://doi.org/10.1529/biophysj.108.135814.

39. Kozakov, D., Brenke, R., Comeau, S.R., and Vajda, S. (2006). PIPER: an FFT-based protein docking program with pairwise potentials. Proteins 65, 392–406. https://doi.org/10.1002/prot.21117.

40. Zhou, J., Liu, C.Y., Back, S.H., Clark, R.L., Peisach, D., Xu, Z., and Kaufman, R.J. (2006). The crystal structure of human IRE1 luminal domain reveals a conserved dimerization interface required for activation of the unfolded protein response. Proc. Natl. Acad. Sci. USA 103, 14343–14348. https://doi.org/10.1073/pnas.0606480103.

41. Li, H., Korennykh, A.V., Behrman, S.L., and Walter, P. (2010). Mammalian endoplasmic reticulum stress sensor IRE1 signals by dynamic clustering. Proc. Natl. Acad. Sci. USA 107, 16113–16118. https://doi.org/10.1073/pnas.1010580107.

42. SWISS-MODEL 2022. https://swissmodel.expasy.org/.

43. Waterhouse, A., Bertoni, M., Bienert, S., Studer, G., Tauriello, G., Gumienny, R., Heer, F.T., De Beer, T.A.P., Rempfer, C., Bordoli, L., et al. (2018). SWISS-MODEL: homology modelling of protein structures and complexes. Nucleic Acids Res. 46, W296–W303. https://doi.org/10.1093/NAR/GKY427.

44. Parkash, V., Lindholm, P., Peränen, J., Kalkkinen, N., Oksanen, E., Saarma, M., Leppänen, V.M., and Goldman, A. (2009). The structure of the conserved neurotrophic factors MANF and CDNF explains why they are bifunctional. Protein Eng. Des. Sel. 22, 233–241. https://doi.org/10.1093/protein/gzn080.

45. Lindholm, P., Voutilainen, M.H., Laurén, J., Peränen, J., Leppänen, V.M., Andressoo, J.O., Lindahl, M., Janhunen, S., Kalkkinen, N., Timmusk, T.,

et al. (2007). Novel neurotrophic factor CDNF protects and rescues midbrain dopamine neurons in vivo. Nature *448*, 73–77. https://doi.org/10.1038/nature05957.

46. Voutilainen, M.H., De Lorenzo, F., Stepanova, P., Bäck, S., Yu, L.Y., Lindholm, P., Pörsti, E., Saarma, M., Männistö, P.T., and Tuominen, R.K. (2017). Evidence for an additive neurorestorative effect of simultaneously administered CDNF and GDNF in hemiparkinsonian rats: implications for different mechanism of action. eNeuro *4*, ENEURO.0117-16.2017. https://doi.org/10.1523/ENEURO.0117-16.

47. Lee, A.-H., Iwakoshi, N.N., and Glimcher, L.H. (2003). XBP-1 regulates a subset of endoplasmic reticulum resident chaperone genes in the unfolded protein response. Mol. Cell Biol. *23*, 7448–7459. https://doi.org/10.1128/mcb.23.21.7448-7459.2003.

48. Amin-Wetzel, N., Neidhardt, L., Yan, Y., Mayer, M.P., and Ron, D. (2019). Unstructured regions in IRE1α specify BiP-mediated destabilisation of the luminal domain dimer and repression of the UPR. Elife *8*, e50793. https://doi.org/10.7554/eLife.50793.

49. Yoshida, H., Matsui, T., Yamamoto, A., Okada, T., and Mori, K. (2001). XBP1 mRNA is induced by ATF6 and spliced by IRE1 in response to ER stress to produce a highly active transcription factor. Cell *107*, 881–891. https://doi.org/10.1016/S0092-8674(01)00611-0.

50. Valdés, P., Mercado, G., Vidal, R.L., Molina, C., Parsons, G., Court, F.A., Martinez, A., Galleguillos, D., Armentano, D., Schneider, B.L., and Hetz, C. (2014). Control of dopaminergic neuron survival by the unfolded protein response transcription factor XBP1. Proc. Natl. Acad. Sci. USA *111*, 6804–6809. https://doi.org/10.1073/pnas.1321845111.

51. Kakazu, E., Mauer, A.S., Yin, M., and Malhi, H. (2016). Hepatocytes release ceramide-enriched pro-inflammatory extracellular vesicles in an IRE1 α -dependent manner. J. Lipid Res. *57*, 233–245. https://doi.org/10.1194/jlr.M063412.

52. Cao, J., Peng, J., An, H., He, Q., Boronina, T., Guo, S., White, M.F., Cole, P.A., and He, L. (2017). Endotoxemia-mediated activation of acetyltransferase P300 impairs insulin signaling in obesity. Nat. Commun. *8*, 131. https://doi.org/10.1038/s41467-017-00163-w.

53. Acosta-Alvear, D., Zhou, Y., Blais, A., Tsikitis, M., Lents, N.H., Arias, C., Lennon, C.J., Kluger, Y., and Dynlacht, B.D. (2007). XBP1 controls diverse cell type- and condition-specific transcriptional regulatory networks. Mol. Cell *27*, 53–66. https://doi.org/10.1016/j.molcel.2007.06.011.

54. Le Thomas, A., Ferri, E., Marsters, S., Harnoss, J.M., Lawrence, D.A., Zuazo-Gaztelu, I., Modrusan, Z., Chan, S., Solon, M., Chalouni, C., et al. (2021). Decoding non-canonical mRNA decay by the endoplasmic-reticulum stress sensor IRE1α. Nat. Commun. *12*, 7310. https://doi.org/10.1038/s41467-021-27597-7.

55. Nishitoh, H., Matsuzawa, A., Tobiume, K., Saegusa, K., Takeda, K., Inoue, K., Hori, S., Kakizuka, A., and Ichijo, H. (2002). ASK1 is essential for endoplasmic reticulum stress-induced neuronal cell death triggered by expanded polyglutamine repeats. Genes Dev. *16*, 1345–1355. https://doi.org/10.1101/gad.992302.

56. Brozzi, F., and Eizirik, D.L. (2016). ER stress and the decline and fall of pancreatic beta cells in type 1 diabetes. Ups. J. Med. Sci. *121*, 133–139. https://doi.org/10.3109/03009734.2015.1135217.

57. Morita, S., Villalta, S.A., Feldman, H.C., Register, A.C., Rosenthal, W., Hoffmann-Petersen, I.T., Mehdizadeh, M., Ghosh, R., Wang, L., Colon-Negron, K., et al. (2017). Targeting ABL-IRE1α signaling spares ER-stressed pancreatic β cells to reverse autoimmune diabetes. Cell Metab. *25*, 883–897.e8. https://doi.org/10.1016/j.cmet.2017.03.018.

58. Kaneko, M., Niinuma, Y., and Nomura, Y. (2003). Activation signal of nuclear factor-κB in response to endoplasmic reticulum stress is transduced via IRE1 and tumor necrosis factor receptor-associated factor 2. Biol. Pharm. Bull. *26*, 931–935. https://doi.org/10.1248/bpb.26.931.

59. Hu, P., Han, Z., Couvillon, A.D., Kaufman, R.J., and Exton, J.H. (2006). Autocrine tumor necrosis factor alpha links endoplasmic reticulum

60. stress to the membrane death receptor pathway through IRE1α-mediated NF-κB activation and down-regulation of TRAF2 expression. Mol. Cell Biol. *26*, 3071–3084. https://doi.org/10.1128/mcb.26.8.3071-3084.2006.

60. Chen, L., Feng, L., Wang, X., Du, J., Chen, Y., Yang, W., Zhou, C., Cheng, L., Shen, Y., Fang, S., et al. (2015). Mesencephalic astrocyte-derived neurotrophic factor is involved in inflammation by negatively regulating the NF-κB pathway. Sci. Rep. *5*, 8133. https://doi.org/10.1038/srep08133.

61. Ghosh, R., Wang, L., Wang, E.S., Perera, B.G.K., Igbaria, A., Morita, S., Prado, K., Thamsen, M., Caswell, D., Macias, H., et al. (2014). Allosteric inhibition of the IRE1α RNase preserves cell viability and function during endoplasmic reticulum stress. Cell *158*, 534–548. https://doi.org/10.1016/j.cell.2014.07.002.

62. Weintraub, M.K., Bisson, C.M., Nouri, J.N., Vinson, B.T., Eimerbrink, M.J., Kranjac, D., Boehm, G.W., and Chumley, M.J. (2013). Imatinib methanesulfonate reduces hippocampal amyloid-beta and restores cognitive function following repeated endotoxin exposure. Brain Behav. Immun. *33*, 24–28. https://doi.org/10.1016/j.bbi.2013.05.002.

63. Kozakov, D., Clodfelter, K.H., Vajda, S., and Camacho, C.J. (2005). Optimal clustering for detecting near-native conformations in protein docking. Biophys. J. *89*, 867–875. https://doi.org/10.1529/biophysj.104.058768.

64. Paschalidis, I.C., Shen, Y., Vakili, P., and Vajda, S. (2007). SDU: a semidefinite programming-based underestimation method for stochastic global optimization in protein docking. IEEE Trans. Automat. Contr. *52*, 664–676. https://doi.org/10.1109/TAC.2007.894518.

65. Morris, G.M., Huey, R., Lindstrom, W., Sanner, M.F., Belew, R.K., Goodsell, D.S., and Olson, A.J. (2009). AutoDock4 and AutoDockTools4: automated docking with selective receptor flexibility. J. Comput. Chem. *30*, 2785–2791. https://doi.org/10.1002/jcc.21256.

66. Biasini, M., Bienert, S., Waterhouse, A., Arnold, K., Studer, G., Schmidt, T., Kiefer, F., Gallo Cassarino, T., Bertoni, M., Bordoli, L., and Schwede, T. (2014). SWISS-MODEL: modelling protein tertiary and quaternary structure using evolutionary information. Nucleic Acids Res. *42*, W252–W258. https://doi.org/10.1093/NAR/GKU340.

67. Banks, J.L., Beard, H.S., Cao, Y., Cho, A.E., Damm, W., Farid, R., Felts, A.K., Halgren, T.A., Mainz, D.T., Maple, J.R., et al. (2005). Integrated modeling program, applied chemical theory (IMPACT). J. Comput. Chem. *26*, 1752–1780. https://doi.org/10.1002/JCC.20292.

68. Bowers, K.J., Chow, E., Xu, H., Dror, R.O., Eastwood, M.P., Gregersen, B.A., Klepeis, J.L., Kolossvary, I., Moraes, M.A., et al. (2006). Scalable algorithms for molecular dynamics simulations on commodity clusters. SC '06 Proc. 2006 ACM/IEEE Conf. Supercomput.

69. Zielkiewicz, J. (2005). Structural properties of water: comparison of the SPC, SPCE, TIP4P, and TIP5P models of water. J. Chem. Phys. *123*, 104501. https://doi.org/10.1063/1.2018637.

70. Zlatic, S.A., Ryder, P.V., Salazar, G., and Faundez, V. (2010). Isolation of labile multi-protein complexes by in vivo controlled cellular cross-linking and immuno-magnetic affinity chromatography. J. Vis. Exp., 1855. https://doi.org/10.3791/1855.

71. McQuin, C., Goodman, A., Chernyshev, V., Kamentsky, L., Cimini, B.A., Karhohs, K.W., Doan, M., Ding, L., Rafelski, S.M., Thirstrup, D., et al. (2018). CellProfiler 3.0: next-generation image processing for biology. PLoS Biol. *16*, e2005970. https://doi.org/10.1371/journal.pbio.2005970.

72. Penttinen, A.M., Suleymanova, I., Albert, K., Anttila, J., Voutilainen, M.H., and Airavaara, M. (2016). Characterization of a new low-dose 6-hydroxydopamine model of Parkinson's disease in rat. J. Neurosci. Res. *94*, 318–328. https://doi.org/10.1002/jnr.23708.

73. Voutilainen, M.H., Bäck, S., Peränen, J., Lindholm, P., Raasmaja, A., Männistö, P.T., Saarma, M., and Tuominen, R.K. (2011). Chronic infusion of CDNF prevents 6-OHDA-induced deficits in a rat model of Parkinson's disease. Exp. Neurol. *228*, 99–108. https://doi.org/10.1016/j.expneurol.2010.12.013.

74. BUTTNER-ENNEVER, J. (1997). The rat brain in stereotaxic coordinates, 3rd edn. By George paxinos and Charles Watson. (Pp. xxxiii+80; illustrated; f$69.95 paperback; ISBN 0 12 547623; comes with CD-ROM.) San diego: academic press. 1996. J. Anat. *191*, 315–317. https://doi.org/10.1046/j.1469-7580.1997.191203153.x.

75. Ungerstedt, U., and Arbuthnott, G.W. (1970). Quantitative recording of rotational behavior in rats after 6-hydroxy-dopamine lesions of the nigrostriatal dopamine system. Brain Res. *24*, 485–493. https://doi.org/10.1016/0006-8993(70)90187-3.

76. Penttinen, A.M., Parkkinen, I., Blom, S., Kopra, J., Andressoo, J.O., Pitkä-nen, K., Voutilainen, M.H., Saarma, M., and Airavaara, M. (2018). Implementation of deep neural networks to count dopamine neurons in substantia nigra. Eur. J. Neurosci. *48*, 2354–2361. https://doi.org/10.1111/ejn.14129.

STAR★METHODS

KEY RESOURCES TABLE

REAGENT or RESOURCE	SOURCE	IDENTIFIER
Antibodies		
anti-MANF	Icosagen	Cat#310-100; RRID: AB_11135308
anti-MANF	R&D Systems	Cat#AF3748; RRID: AB_2059299
anti-TH	Millipore	Cat#MAB318; RRID: AB_2201528
anti-TH	Pel-Freez Biologicals	Cat#P40101; RRID: AB_2313713
anti-IRE1α	Cell Signaling Technology	Cat#3294; RRID: AB_823545
anti-pSer724-IRE1α	NovusBio	Cat#NB100-2323; RRID: AB_10145203
anti-HA	Abcam	Cat#ab130275; RRID: AB_11156884
anti-BiP	Cell Signaling Technology	Cat#3177; RRID: AB_2119845
anti-GRP78 BiP	Abcam	Cat#ab21685; RRID: AB_2119834
anti-α-Tubulin	Sigma-Aldrich	Cat#T9026; RRID: AB_477593
anti-PDI	Enzo Life Sciences	Cat#SPA-891-488F; RRID: AB_1193526
anti-rabbit IgG (H + L) Alexa Fluor 488	Invitrogen	Cat#A-11008; RRID: AB_143165
anti-mouse IgG (H + L) Alexa Fluor 568	Invitrogen	Cat#A-11004; RRID: AB_2534072
anti-DAT	Santa Cruz Biotechnology	Cat#sc-32258; RRID: AB_627400
anti-rabbit IgG (H + L) biotinylated	Vector Laboratories	Cat#BA-1000; RRID: AB_2313606
anti-rat IgG (H + L)	Vector Laboratories	Cat#BA-9400; RRID: AB_2336202
anti-mouse IgG (H + L)	Vector Laboratories	Cat#BA-2001; RRID: AB_2336180
anti-goat IgG/HRP	Agilent	Cat#P0449; RRID: AB_2617143
anti-Venus	MyBioSource	Cat#MBS448126
Normal goat IgG Control	R&D Systems	Cat#AB-108-C; RRID: AB_354267
Bacterial and virus strains		
DH5α	Thermo Fisher Scientific	Cat#18265017
Chemicals, peptides, and recombinant proteins		
FBS	Gibco	Cat#10270106
Ham's F12 nutrient mix	Thermo Fisher Scientific	Cat#21765029
GlutaMAX	Thermo Fisher Scientific	Cat#35050061
JetPEI	Polyplus Transfections	Cat#101–10N
Hygromycin Gold	Invivogen	Cat#ant-hg-1
DMEM	Lonza	Cat#BE12-614F
MEM Non-Essential Amino Acids	Gibco	Cat#11140035
KIRA6	MedChemExpress	Cat#HY-19708
4μ8C	Cayman Chemical	Cat#14003-96-4
Casein	Sigma-Aldrich	Cat#C8654
Tween 20	Sigma-Aldrich	Cat#P2287
Normocin	InvivoGen	Cat#ant-nr-2
Thapsigargin	Thermo Fisher Scientific	Cat#T7459
Tunicamycin	Abcam	Cat#ab120296
C-MANF	Apeptide	N/A
IRE1α	Icosagen	N/A
Mutated hIRE1α-His	Icosagen	N/A
PERK	Icosagen	N/A
ATF6	Icosagen	N/A
MANF	Icosagen	Cat#P-101-100
GRP78 (BiP)	StressMarq Biosciences	Cat#SMB-SPR-119A

(Continued on next page)

Continued

REAGENT or RESOURCE	SOURCE	IDENTIFIER
PNGase F	New England Biolabs	Cat#P0704S
Turbofect	ThermoFisher Scientific	Cat#R0531
Poly-D-Lysine	Sigma-Aldrich	Cat#P0899
DAPI	Sigma-Aldrich	Cat#D9542
Triton X-100	Sigma-Aldrich	Cat#T9284
ProLong Diamond Antifade Mountant	ThermoFisher Scientific	Cat#P36965
PEI Transfection Reagent	Polysciences	Cat#23966–100
Doxycycline	Sigma-Aldrich	Cat#D3447
PhosSTOP	Roche	Cat#4906845001
cOmplete™, EDTA-free Protease Inhibitor Cocktail	Roche	Cat#04693132001
BSA	Sigma-Aldrich	Cat#A8806
TRI reagent	Invitrogen	Cat#AM9738
Maxima H Minus Reverse Transcriptase	Thermo Fisher Scientific	Cat#EP0753
dNTP mix	Fermentas UAB	Cat#R01936
Trypsin	MP Biomedical	Cat#103139
HBSS (Ca^{2+}/Mg2+-free)	Invitrogen	Cat#14170112
poly-DL-ornithine	Sigma-Aldrich	Cat#P8638
6-OHDA	Sigma Chemical	Cat#H-4381
Sodium pentobarbital	Orion Pharma	N/A
Normal horse serum	Vector Laboratories	Cat#S-2000
3, 3′-diaminobenzidine (DAB)	Vector Laboratories	Cat#SK-4100
Dextran Texas Red	Invitrogen	Cat#D1864
polyornithine-laminin	Sigma-Aldrich	Cat#P3655
polyornithine-laminin	Sigma-Aldrich	Cat#CC095
NGF	Promega	Cat#G5141
B27 supplement	Invitrogen	Cat#17504044
Dextran Texas Red	Invitrogen	Cat#D1864
DharmaFECT reagent	Horizon Discovery	Cat#T-2001-01
siGENOME Human MANF (7873) siRNA – SMARTpool	Horizon Discovery	Cat#M-012158-03–0005
siGENOME Non-Targeting siRNA Control Pool #1	Horizon Discovery	Cat#D-001206-13-05
Dynabeads Protein G	Invitrogen	Cat#10004D
Critical commercial assays		
Lightcycler 480 SYBR Green I Master mix	Roche Diagnostics	Cat#04887352001
Elite ABC Vectastain kit	Vector Laboratories	Cat#PK-6102
ER-ID Red assay kit	Enzo Life Sciences	Cat#ENZ-51026-K500
Monolith His-Tag Labeling Kit RED-tris-NTA	NanoTemper Technologies GmbH	Cat#MO-L008
Duoset ELISA Development System	R&D Systems	Cat#DY999
mini-PROTEAN precast gels	Bio-Rad	Cat#456–1093
Phos-tag acrylamide	Fujifilm Wako Chemicals	Cat#AAL-107S1
Duolink	Sigma-Aldrich	Cat#DUO92008
DC protein assay (Bio-Rad)	Bio-Rad	Cat#5000112
Lightcycler 480 SYBR Green I Master mix	Roche Diagnostics	Cat#04887352001
Experimental models: Cell lines		
Flp-In T-REx 293	Thermo Fisher Scientific	Cat#R78007
Flp-In IRE1α-HA T-REx 293	This study	N/A
Flp-In BiP-HA T-REx 293	This study	N/A

(*Continued on next page*)

Continued

REAGENT or RESOURCE	SOURCE	IDENTIFIER
Flp-In GFP-HA T-REx 293	This study	N/A
T-Rex293T::IRE1a-GFP	Laboratory of Peter Walter (Li et al., 2010)[41]	N/A
Flp-In-CHO	Thermo Fisher Scientific	Cat#R75807
pre-SH-MANF-CHO	This study	N/A
pre-SH-IRE1α-CHO	This study	N/A
pre-SH-BiP-CHO	This study	N/A
GFP-SH-CHO	This study	N/A
IRE1a−/−::IRE1a-HA MEFs	Laboratory of David Ron	N/A
IRE1a−/−::EV MEFs	Laboratory of David Ron	N/A
QMCF CHO 1E9	Icosagen	N/A
Experimental models: Organisms/strains		
Male Wistar rats	Envigo	RRID: RGD_38548927
NMRI mice	Envigo	RRID: MGI:5658486
Oligonucleotides		
See Table S8 for the primers used in the study	(Pakarinen et al., 2020)[15]	N/A
Recombinant DNA		
pCE-BiFC-VC155 (CV)	Addgene	Cat#22020
pCE-BiFC-VN173 (NV)	Addgene	Cat#22019
PEZYflag	Addgene	Cat#18700
pEZYmyc-His	Addgene	Cat#18701
pENTR221	Invitrogen	Cat#12536017
pDONR223-ERN1	Addgene	Cat#23491
pEZY BiFC N NV	This study	N/A
pEZY BiFC N CV,	This study	N/A
pEZY BiFC C NV	This study	N/A
pEZY BiFC C CV	This study	N/A
pCR3.1 MANF	(Hellman et al., 2011)[14]	N/A
pDONR223 pre-CV-IRE1	This study	N/A
pEZY BiFC BiP NBD-NV	This study	N/A
pEZY BiFC BiP SBD-NV	This study	N/A
pEZY BiFC pre-NV-MANF	This study	N/A
pEZY BiFC pre-NV-C-MANF	This study	N/A
pEZY BiFC pre-NV-N-MANF	This study	N/A
cDNA synthesis	Genewiz	N/A
pQMCF-1T-Amp-R5	Icosagen	N/A
Software and algorithms		
Graphpad Prism 7	https://www.graphpad.com/scientific-software/prism/	RRID: SCR_015807
ImageJ	https://imagej.nih.gov/ij/	RRID: SCR_003070
Monolith	https://nanotempertech.com/monolith/	N/A
MO.Affinity Analysis (x86)	https://nanotempertech.com/monolith/	N/A
MO.Control	https://nanotempertech.com/monolith/	N/A
CellProfiler 3.1.5	http://www.cellprofiler.org	RRID: SCR_007358
CellProfiler-Analyst-2.2.1	http://www.cellprofiler.org	RRID: SCR_007358
Leica Application Suite X (LASX)	Leica Microsystems Inc	N/A
LAS AF 1.82	Leica Microsystems Inc	N/A
CorelDRAW 2018	https://www.coreldraw.com/en/	RRID: SCR_014235

Continued

REAGENT or RESOURCE	SOURCE	IDENTIFIER
Imaris 9.2.1 software (Bitplane)	Oxford Instruments	N/A
CNN algorithm and supervised learning	MathWorks	N/A
Image-Pro Plus software (version 3.0.1; Media Cybernetics)	https://www.mediacy.com/imageproplus	RRID: SCR_016879
Schrödinger LLC Maestro	Schrödinger, LLC	N/A
Impact, Schrödinger, LLC	Schrödinger, LLC	N/A
BioLuminate software, Schrödinger LLC	Schrödinger, LLC	N/A
AutoDock Tools	https://autodock.scripps.edu	RRID: SCR_012746
SWISS-MODEL server	https://swissmodel.expasy.org	N/A
Desmond	Schrödinger, LLC	N/A
Image Lab	Bio-Rad	N/A
Other		
Panoramic P250 Flash II whole slide scanner (3DHistech, Budapest, Hungary)	3DHistech, https://epredia.com/about/	N/A
Cryomicrotome (Leica Instruments)	Leica Microsystems	N/A
Aiforia image processing and management platform	Aiforia Oy	N/A
Automatic rotometer bowls (Med Associates)	Med Associates	N/A
CellInsight high-content imaging equipment	ThermoFisher Scientific	N/A
NanoDrop 2000 spectrophotometer	ThermoFisher Scientific	N/A
OptiPlate-96 Black, Black Opaque 96-well Microplate	Perkin Elmer	Cat#6005270
Amicon Ultra-4 centrifugal filters 10K	Merk Millipore	Cat#UFC903008
Superdex 200 Increase 3.2/300 column	GE Healthcare	Cat#28990946
Premium coated capillaries	NanoTemper Technologies GmbH	Cat#MO-K025
Nickel-coated plates	Pierce	Cat#15442
Plate reader	VICTOR3, Perkin Elmer	N/A
Leica SP8 STED confocal microscope	Leica Microsystems Inc	N/A
MolecularDevices Nano scanner	Molecular Devices, LCC	N/A
Lightcycler 480 Real-Time PCR System (Roche)	Roche	N/A
Confocal microscope TCS SP5	Leica Microsystems Inc	N/A
Leica HCX PL APO x63/1.3 GLYC CORR CS (21°C) objective	Leica Microsystems Inc	N/A
HisTrap Excel column	Cytiva	Cat#GE17-5255-01

RESOURCE AVAILABILITY

Lead contact
Further information and requests for resources and reagents should be directed to and will be fulfilled by the lead contact, Mart Saarma (mart.saarma@helsinki.fi).

Materials availability
Plasmids and cell lines generated in this study will be available upon request.

Data and code availability
- All data reported in this paper will be shared by the lead contact upon request.
- This paper does not report original code.
- Any additional information required to reanalyze the data reported in this paper is available from the lead contact upon request.

EXPERIMENTAL MODEL AND SUBJECT DETAILS

Experimental animals

8 weeks old male Wistar rats (weight 230–270 g, Envigo, Netherlands) were housed in groups of 3–4 under a 12 h light-dark cycle at an ambient temperature of 20–23°C. Food pellets (Harlan Teklad Global diet, Holland) and tap water were available *ad libitum*. Experiments were performed according to the 3R principles of EU directive 2010/63/EU on the care and use of experimental animals, as well as local laws and regulations, and were approved by the national Animal Experiment Board of Finland (protocol approval number ESAVI/12830/2020). All experiments were performed in a blinded manner and the rats were assigned to the treatment groups equally based on their rotational score at week 2.

Primary cell cultures

Culture of mouse SCG sympathetic neurons and microinjection of these neurons were performed as described earlier [80]. Briefly, the neurons of NMRI strain mice (P1-P2, sex was not determined) were grown for 6 days on polyornithine-laminin (P3655 and CC095, Sigma-Aldrich)–coated dishes or glass coverslips with 30 ng/mL of 2.5 S mouse NGF (G5141, Promega) in the Neurobasal medium containing B27 supplement (17504044, Invitrogen).

The midbrain floors were dissected from the ventral mesencephalic of NMRI strain mouse embryos (E13, sex of the embryos was not determined). The tissues of the midbrain floors were incubated with 0.5% trypsin (103139, MP Biomedical) in HBSS (Ca^{2+}/Mg^{2+}-free) (14170112, Invitrogen) for 20 min at 37°C, then mechanically dissociated. Cells were plated on the 96-well plates coated with poly-L-ornithine (Sigma-Aldrich). Equal volumes of cell suspension were plated onto the center of the dish. The cells were grown for 5 days without any added neurotrophic factor in DMEM/F12 medium containing N-2 supplement (17502048, Invitrogen). Neuronal cultures were maintained at 37°C and 5% CO_2. Primary cultures were prepared following European Community guidelines for the use of experimental animals and approved by the Finnish National Experiment Board (License number: ESAVI/12830/2020) and also by the Laboratory Animal Center of the University of Helsinki (license no. KEK20-015; 2.7.2020).

Cell lines

HEK293 cells for bimolecular fluorescence complementation assay (BiFC) experiments were grown in Dulbecco's modified Eagle's medium (DMEM), supplemented with 10% fetal bovine serum (FBS) (10270106, Gibco) and 50 μg/mL normocin (ant-nr-2, InvivoGen). HEK293 cells used for siRNA transfection and crosslinking co-IP experiments were grown in Minimum Essential Media (MEM 61100-087, Gibco) with 10% fetal bovine serum (FBS) (10270106, Gibco) and 50 μg/mL normocin (ant-nr-2, InvivoGen). HEK293 cells and other cell lines used were grown at 37°C and 5% CO_2.

Flp-In T-REx 293 cell line (Invitrogen) containing a single stably integrated FRT site and expressing Tet repressor were used for generation of inducible cell lines, expressing IRE1α-HA, BiP-HA or GFP-HA. The medium composition was the same as for HEK293 cells.

Flp-In-CHO cells (R75807, Thermo Fisher Scientific) were grown in growth media consisting of Ham's F12 nutrient mix (21765029, Thermo Fisher Scientific), 10% FBS, 2mM GlutaMAX (35050061, Thermo Fisher Scientific) and normocin (ant-nr-2, Invivogen). We used the Flp-In-CHO to generate CHO-derived stable transgenic cell lines overexpressing either MANF or its mutants from a transcriptionally active locus. For this, the respective pcDNA5/FRT/TO pre-SH-MANFwt or mutant constructs were co-transfected with the Flp-recombinase expressing pOG44 plasmid in a 1:9 ration using JetPEI (101-10N, Polyplus Transfections) transfection reagent. The selection was started 48 h after transfection using growth media supplemented with 500 μg/mL Hygromycin Gold (ant-hg-1, Invivogen). Selection media was changed every 3–4 days until confluent colonies of stable transgenic cells had formed and cells were ready to be split.

MEFs were grown in DMEM (12-614F, Lonza), supplemented with 5% FBS (10270106, Gibco) and 1% non-essential amino acids (11140035, Gibco) at 37°C and 5% CO2.

METHOD DETAILS

Reagents and proteins

The inducers of ER stress thapsigargin (T7459, ThermoFisher Scientific) and tunicamycin (ab120296, Abcam) and IRE1α inhibitors KIRA6 (HY-19708, MedChemExpress) and 4μ8C (14003-96-4, Cayman Chemical) were used.

LDs of three UPR sensors, human IRE1α, PERK and ATF6 and human MANF, as well as MANF mutant and IRE1α LD mutant proteins were expressed and purified in CHO cells by Icosagen Ltd. (Tartu, Estonia). Human C-MANF was expressed and purified from *E.coli* cells, as described in[14] or synthesized chemically by Apeptide Ltd. (Shanghai, China). Human recombinant GRP78 (BiP) was obtained from StressMarq Biosciences Inc. (SMB-SPR-119A).

Microscale thermophoresis (MST)

The experiments have been performed using Monolith NT.115 instrument (NanoTemper Technologies GmbH, Germany). Recombinant proteins were labeled through His-tag using Monolith His-Tag Labeling Kit RED-tris-NTA (MO-L008). The concentration of labelled proteins (targets) was 20 nM for all the experiments while different starting concentrations of the ligand series were used depending on the experiment.

Experiments were performed in a buffer containing 10 mM Na-phosphate buffer, pH 7.4, 1 mM MgCl$_2$, 3 mM KCl, 150 mM NaCl, 0.05% Tween-20. The measurements were done in premium coated capillaries (NanoTemper Technologies GmbH, MO-K025) using red LED source, power set at 100% and medium MST power at 25°C. 12–14 data points, corresponding different ligand concentrations, were used per binding curve. Each data point represents mean fraction bound or ΔF_{norm} values from n = 3–5 independent experiments per binding pair ± S.D, K_d values ± error estimations are indicated. Data analysis was performed using MO.Affinity Analysis v2.3 and GraphPad Prism 7 software.

Binding assay on nickel-coated plates

Nickel-coated plates (15,442, Pierce) were blocked with 1% casein in PBS-T for 1 h at room temperature (RT). The mixtures of BiP-His + MANF (positive control), IRE1α LD-His + MANF and GFRα1-His + MANF (negative control) were prepared at the 1:1 ratio in the buffer, that was used for MST experiments with following incubation for 1 h at RT. MANF + buffer mix was used as background control. After the incubation protein solutions were pipetted on the plates and incubated on the plates for 1 h at RT. The plates were washed 3 times with 0.05% Tween-20 (P2287, Sigma-Aldrich) in PBS. After washing the plates were incubated with the HRP-linked mouse anti-human MANF, clone 4E12 (Icosagen) antibody overnight at 4°C on a shaker. Next day the plates were washed 3 times and the color development was performed using Duoset ELISA Development System (DY999, R&D Systems) according to the manufacturer's instructions. The absorbance at 450 and 540 nm was measured using plate reader (VICTOR3, Perkin Elmer). The background absorbance was subtracted. Data analysis was performed using GraphPad Prism 7 software.

Analysis of purity and glycosylation of LDs of UPR sensors

The PNGase F (P0704S, New England Biolabs) was used for analysis of protein N-glycosylation and the assay was performed according to the manufacturer's instructions. Glycosylated (5μg/well) versus deglycosylated proteins were loaded onto mini-PROTEAN precast gels (456–1093, Bio-Rad) and run at 40 mA for 1 h. Coomassie Brilliant Blue G-250 staining was performed according to the standard protocol. Glycosylated mammalian cell-produced GDNF protein was used as a positive control.

Size exclusion chromatography

For complex preparation, purified human CHO-expressed MANF and IRE1α LD were combined in a molar ratio of 1.25:1 (MANF:IRE1α LD) at a total protein concentration of 0.7 mg/mL in size exclusion chromatography buffer (10 mM MES-NaOH, pH 5.5, 150 mM NaCl, 3 mM KCl, 1 mM MgCl$_2$, 0.05% Tween-20). The complex was incubated for 10 min at 22°C before size exclusion chromatography using a Superdex 200 Increase 3.2/300 column (GE Healthcare) at 22°C. Individual components were also run similarly. Selected fractions were analyzed by WB.

Protein – protein docking

The crystal structure of the human IRE1α LD (PDB ID: 2HZ6) at 3.1 Å resolution,[40] the structure with the least restraint violations from the NMR solution structure of the C-terminal domain of MANF (PDB ID: 2KVE),[14] and crystal structure of full-length MANF (PDB ID: 2W51)[44] were used for protein–protein docking. Before the docking procedure, 3D structures of proteins were optimized using the Protein Preparation Wizard (OPLS_2005 force field) in the Schrödinger LLC Maestro software (Schrödinger Release 2018-3: Schrödinger Suite 2018-3 Protein Preparation Wizard; Epik, Schrödinger, LLC, New York, NY (2018); Impact, Schrödinger, LLC, New York, NY, 2018; Prime, Schrödinger, LLC, New York, NY (2018)). The protein-protein docking was carried out using PIPER procedure of BioLuminate software, Schrödinger LLC (Schrödinger Release 2018-3: BioLuminate, Schrödinger, LLC, New York, NY (2018)), which proceeds with a rigid body global search based on the fast Fourier transform correlation approach.[39] The PIPER procedure performs exhaustive evaluation of an energy function based on DARS (Decoys As the Reference State) potentials[38] in discretized 6D space of mutual orientations of two proteins. The structures corresponding to different mutual orientations of the proteins were ordered according to the scoring function that is given as the sum of terms representing shape complementarity, electrostatic, and desolvation contributions (desolvation is taken into account by semiempirical term in the potential function). The top 1000 structures were subsequently clustered using the pairwise root mean square deviation as the distance measure between two proteins in the complex within a fixed clustering radius 9 Å.[63] The selected structures from the 30 largest clusters that represent the most likely computational models of the complex structure were refined using the Semi-Definite programming based Underestimation medium-range optimization method.[64] The analysis of the protein – protein interactions of the final 30 top models was performed by using AutoDock Tools software.[65]

Homology modelling and optimization of the full-length structure of IRE1α LD

The homology modelling of the 3D structure of IRE1α LD containing intrinsically disordered regions (residues V308 – N357), absent on crystal structure (PDB ID: 2HZ6),[40] was carried out using the SWISS-MODEL server.[42,43] The amino acid sequence of IRE1α LD in FASTA format was retrieved from Protein Data Bank.[40] The SWISS-MODEL performs homology modelling using the following steps: (1) input data; (2) template search; (3) template selection; (4) model building, and (5) model quality estimation.[43] The generated 3D model of IRE1α LD with higher QMEAN and GMQE values[66] was selected for further modelling (model **1**, Figures S4C and S4D). At first, the predicted model of IRE1α LD was prepared using the Protein Preparation Wizard (OPLS_2005 force field[67]) in the Schrödinger LLC Maestro software (Schrödinger Release 2018-3: Schrödinger Suite 2018-3 Protein Preparation Wizard; Epik,

Schrödinger, LLC, New York, NY (2018); Impact, Schrödinger, LLC, New York, NY, 2018; Prime, Schrödinger, LLC, New York, NY (2018)). The modeled structure is a homodimer of IRE1α LD, with individual protein molecules denoted as chain A and chain B (Figure S4D). For modelling purposes, only a single IRE1α LD chain is needed, thus just chain A was used. Thereafter, in order to optimize the predicted structure and minimize its energy, the molecular dynamics (MD) simulation with length 50 ns using Desmond simulation package of Schrödinger LLC[68] was carried out. The 3D model of IRE1α LD was solvated in a cubic simple point-charge (SPC)[69] water box using OPLS_2005 force field parameters.[67] The NaCl salt was placed in the solvent to a concentration 0.15 M, and then, to achieve electroneutrality, counter-ions were added to the system. The quality of MD simulations was analyzed using the Simulation Quality Analysis tool implemented in Desmond molecular dynamics package. The root mean square deviation (RMSD) of the Cα atom positions in time was used for the monitoring of the stability of the predicted structure of IRE1α LD. The structure of IRE1α LD corresponding to the 50 ns time-point of MD simulation was saved in a separate PDB file and used for protein-protein docking. The MD results are presented in Figure S4E.

Knockdown of MANF using siRNA

HEK293 cells were plated in 12-well plates, 2.8×10^5 cells/well, and transfected in the following day according to manufacturer's protocol using DharmaFECT reagent and siGENOME Human MANF (7873) siRNA – SMARTpool, to knockdown MANF, or with siGENOME Non-Targeting siRNA Control Pool #1 (Dharmacon, Horizon Discovery). After 48 h, cells were lysed with RIPA buffer (25 mM Tris-HCl, pH7.5, 150 mM NaCl, 1% NP-40, 0.5% sodium deoxycholate, 0.1% SDS) containing cOmplete™, EDTA-free Protease Inhibitor Cocktail and PhosSTOP phosphatase inhibitor (Roche). Protein concentration was determined using DC protein concentration assay (Bio-Rad). Samples were run in 4–15% Mini-PROTEAN® TGX™ Precast Protein Gels (Bio-Rad), 20 μg/lane, blotted, and probed with following antibodies: goat anti-MANF (1:1000, R&D AF3748), rabbit anti-IRE1α (1:1000, Cell Signaling Technology, 3294) and mouse anti-α-Tubulin (1:1000, Sigma-Aldrich, T9026).

Crosslinking and co-immunoprecipitation (co-IP)

Crosslinking of multiprotein complexes in HEK293 cells followed by anti-MANF co-IP was performed essentially according to.[70] To study MANF immunocomplexes during ER stress, HEK293 cells were plated in 6 cm dishes at density of 1.4×10^5 cells/cm^2 and treated 24-40 h later either with tunicamycin (2.5 μg/mL) or thapsigargin (1 μM) for 1 h, 4 h or 20 h to induce ER stress, or with DMSO as a control. To crosslink protein complexes, cells were placed on ice and incubated with DSP (dithiobis(succinimidyl propionate)) crosslinker solution (1 mM DSP in PBS with 0.1 mM CaCl$_2$ and 1 mM MgCl$_2$) for 2 h. After quenching the reaction with 20 mM Tris pH 7.4 in PBS/Ca/Mg for 15 min, cells were lysed for 30 min on ice with Buffer A (10 mM HEPES, pH 7.4, 150 mM NaCl, 1 mM EGTA, 0.1 mM MgCl$_2$) containing 0.5% Triton X-100, and cOmplete™, EDTA-free Protease Inhibitor Cocktail (Roche). Samples were centrifuged at 15.000xg for 15 min at 4°C, supernatants collected and protein concentration determined using DC protein assay (Bio-Rad).

For co-IP, 1.5 μg goat anti-human MANF antibodies (AF3748; R&D) or normal goat IgG (R&D) as a negative control were added to crosslinked HEK293 lysate containing about 500 μg of protein, and incubated in end-over-end rotation o/n at 4°C. Next day, 15 μL of Dynabeads Protein G was added and samples were incubated for additional 2 h to collect immunocomplexes. Dynabead-immunocomplexes were washed 6x with Buffer A containing 0.1% Triton X-100, and cOmplete™, EDTA-free Protease Inhibitor Cocktail (Roche). Proteins were eluted with reducing Laemmli buffer and heating at 95°C for 5 min. Eluates were run in 4–15% Mini-PROTEAN® TGX™ Precast Protein Gels (Bio-Rad), blotted on 0.45 μm nitrocellulose membrane and probed with goat anti-MANF (1:1000, R&D AF3748), rabbit anti-IRE1α (1:1000, Cell Signaling Technology, #3294) and rabbit anti-BiP (1:1000, Abcam, ab21685) antibodies. ECL signal was detected and quantified using Image Lab software (Bio-Rad).

Analysis of IRE1α phosphorylation

Phosphorylated IRE1α (P-IRE1α) in protein lysates from HEK293 cells was detected using Phos-tag SDS-PAGE. Samples were applied in 5% Phos-tag SDS-PAGE gels containing 25 μM Phos-tag acrylamide (Fujifilm Wako Chemicals) and 50 μM MnCl$_2$, and run at 100 V for 2.5 h. Before transfer, gels were incubated in blotting buffer containing 10 mM EDTA for 10 min to chelate Mn^{2+} ions, and rinsed in EDTA-free blotting buffer for 10 min. Samples were blotted to nitrocellulose membrane, and P-IRE1α and IRE1α were detected with antibodies to IRE1α (1:1000; 3294; Cell Signaling Technology).

Generation of MANF mutant plasmids and recombinant proteins

pcDNA5/FRT/TO pre-SH-MANF K96A, C130S and R155A mutants were generated using site-directed inverse PCR mutagenesis and pcDNA5/FRT/TO pre-SH-MANF as template. The pcDNA5/FRT/TO pre-SH-MANF K128AC130S mutant was generated using pcDNA5/FRT/TO pre-SH-MANF C130S as template.

Recombinant human MANF protein was produced from a CHO-derived cell line using the QMCF technology as has been described before (P-101-100, Icosagen). The MANF K96A and K128AC130S mutant recombinant proteins were produced by Icosagen using the same technology. Briefly, codon-optimized cDNAs were cloned to pQMCF-T expression vectors which were then transiently transfected to CHO-derived protein production cell line. Proteins were captured and purified from the cell culture media using 5 mL Q FF followed by 1 mL SP HP, buffer was exchanged into PBS, pH 7.4, by size exclusion chromatography. Protein purity was verified by SDS-PAGE with Coomassie staining and immunoblotting using rabbit anti-MANF antibody (#310-100, Icosagen).

Generation of IRE1α LD mutant plasmids and recombinant proteins

The mutated hIRE1α-His sequences were sent to Icosagen Ltd. (Tartu, Estonia). cDNAs synthesis was ordered from Genewiz. cDNAs were cloned into pQMCF-1T-Amp-R5 vector, plasmids were purified and mutated hIRE1α-His cDNAs were sequenced. Plasmids were transfected into QMCF CHO 1E9 cells for transient production in 600 mL culture volume. Clarified and filtered cell culture supernatants were and loaded onto HiTrap Excel column. Total protein concentration in eluted fractions were measured by NanoDrop 2000 C A280. Fractions were analyzed on SDS-PAGE by Coomassie staining. Purified proteins were desalted into PBS pH 7.5. Purified proteins were sterile filtered, concentration was measured by NanoDrop 2000 C A280 using specific coefficient, adjusted to 1 mg/mL, aliquoted and frozen in liquid nitrogen. Purified proteins were analyzed under non-redued and reduced conditions by Coomassie staining, 2 μg was loaded on lane (Figure S4B).

Duolink proximity ligation assay (PLA)

The experiments were performed in 96-well format on Flp-In T-REx 293 cells, expressing IRE1α-HA/BiP-HA/GFP-HA upon doxycycline induction or on CHO cells, stably expressing HA-tagged MANF. 1×10^4 cells/well were plated on pre-coated with poly-D-lysine (0.1 mg/mL) black Perkin Elmer plates. Cells were fixed with 4% paraformaldehyde for 15 min and afterwards permeabilized / stained with DAPI (D9542, Sigma-Aldrich) in 1 x PBS containing 0.05% Triton X-100 for 10 min. Blocking and incubation with antibodies have been performed following Duolink manufacturer's protocol. Cells were incubated overnight at 4°C with the following primary antibodies: anti-MANF rabbit pAb (Icosagen, #310-100), anti-IRE1α rabbit mAb (CST, #3294), anti-BiP rabbit mAb (CST, #3177), anti-HA mouse mAb (Abcam, ab130275). Incubation with PLUS and MINUS PLA probes have been performed for 1 h at 37°C. Ligation and amplification was performed according to manufacturer's instructions. The imaging of 16 sites/well was performed in TexasRed and DAPI channels using MolecularDevices Nano scanner. The analysis and quantification was done using CellProfiler 3.1.5 and CellProfiler Analyst 2.2.1 software.[71]

Plasmids for bimolecular fluorescence complementation assay (BiFC)

pCE-BiFC-VC155 (CV) and pCE-BiFC-VN173 (NV) were a gift from Chang-Deng Hu (Addgene plasmids #22020 and #22019). pEZY-flag and pEZYmyc-His were a gift from Yu-Zhu Zhang (Addgene plasmids #18700 and #18701). Gateway destination vectors for BiFC for N- and C-terminal tagging with Venus fluorescent protein fragments (pEZY BiFC N NV, pEZY BiFC N CV, pEZY BiFC C NV and pEZY BiFC C CV) were generated by PCR by replacing the flag or myc-His sequences from pEZYflag or pEZYmyc-His with VC155 or VN173 sequences from the respective plasmids.

To generate the MANF Gateway compatible entry vector, pCR3.1 MANF[14] was used to clone the MANF coding region into pENTR221 vector using Gateway entry clone generation by PCR, following the manufacturer's instructions (Invitrogen, Thermo Fisher Scientific, USA).

The following Gateway entry clones were from the Genome Biology Unit (GBU) Core Facility (Research Programs Unit, Faculty of Medicine, HiLIFE, University of Helsinki, Biocenter Finland): HSPA5 (BiP) without stop (DQ895368), JUN without stop (DQ896432), FOS without stop (DQ893444), MAX without stop (JF432558). Shown is the Genbank accession number and the presence or absence of a translation stop codon to indicate subsequent N- or C-terminal fusion, respectively, with a Venus fragment. The corresponding BiFC expression plasmids were made by LR clonase recombination reaction of pENTR221 constructs into the respective pEZY BiFC destination vector. pDONR223-ERN1 (IRE1) was a gift from William Hahn & David Root (Addgene plasmid # 23491). A stop codon at the end of the IRE1-coding reading frame was added before using that construct to generate a pDONR223 pre-CV-IRE1. For that purpose, inverse PCR was used to linearize the pDONR223 IRE1 with stop construct between the sequences corresponding to the pre-sequence and the mature IRE1. A C-Venus insert with a GS-linker was amplified from a pEZY BiFC pre-CV containing construct and used in a ligation reaction with the linearized pDONR223 IRE1 stop construct to generate pDONR223 pre-CV-IRE1. The latter was then used as an entry clone in an LR reaction to recombine the pre-CV-IRE1 sequence into the pEZY BiFC myc-His destination vector.

pEZY BiFC BiP NBD-NV and Grp78 SBD-NV were made using BiP NBD and SBD specific primers for inverse PCR and pEZY BiFC BiP-NV was used as a template.

pENTR221 pre-N-Venus MANF was generated by amplifying the sequence corresponding to VN173 from the respective BiFC destination vectors and inserting it between the sequences coding for signal peptide (pre) and mature regions of human pENTR221 MANF. The corresponding BiFC expression plasmids (pEZY BiFC pre-NV-MANF) were made by LR clonase recombination reaction of pENTR221 pre-NV-MANF into pEZY Myc-His destination vector.

pEZY BiFC pre-NV-N-MANF and pre-NV-C-MANF constructs were generated using inverse PCR reactions the N-MANF or C-MANF specific primers, respectively and the pEZY BiFC pre-NV-MANF as a template.

BiFC and immunocytochemistry

HEK293 cells were plated on covered with poly-D-lysine (P0899, Sigma-Aldrich) coverslips and thereafter were co-transfected with pEZY BIFC N-Venus and C-Venus plasmids 48 h after plating. Transfection with jetPEI transfection reagent (101, Polyplus-transfecton) was performed according to the manufacturer's protocol. The cells were transfected with bait and prey proteins fused either to the N-terminal (NV) or C-terminal (CV) fragment of Venus. Bait and prey proteins' interaction, enables the detection of binding using fluorescence microscopy. To ensure the correct cellular localization of tested proteins the Venus fragments were located between

the signal sequences and mature proteins. As positive controls, we used a pair of interacting transcription factors Jun and Fos, and BiP as a known interactor of IRE1α LD. To check for the absence of a non-specific background signal, we tested the interaction between non-interacting Jun and Max.

20 h after transfection the cells were fixed with 4% PFA, washed with PBS and permeabilized using 0.1% Triton X-100 in PBS (PBS-T). The ER-ID Red assay kit (ENZ-51026-K500, Enzo Life Sciences), containing Hoechst 33342 nuclear stain and ER-ID Red detection reagent was used for nuclear and endoplasmic reticulum staining. ProLong Diamond Antifade Mountant (P36965, ThermoFisher Scientific) was used for mounting of coverslips. The imaging was performed using Leica SP8 STED confocal microscope, 63x glycerol immersion objective and Leica Application Suite X (LASX) software. Image analysis and processing (including brightness / contrast adjustment, same for all images) was done using CorelDRAW 2021.

For immunocytochemistry in addition to Hoechst 33342 for nuclear staining and ER-ID Red for ER staining, anti-Venus (Mybiosource, MBS448126) (1:500) primary antibodies and Alexa Fluor 488 (1:500) anti-goat secondary antibodies were used. The imaging was performed using Olympus BX61 fluorescent microscope. Image processing was done using CorelDRAW 2021.

IRE1α oligomerization assay

TREx-293IRE1α-3FGHGFP cells[41] were plated 5 × 10³ cells/well on pre-coated with poly-D-lysine (0.1 mg/mL) black Perkin Elmer plates in DMEM with 10% FBS and 100 μg/mL normocin. Next day the cells were transiently transfected with pTO-pre-SH-MANF-GW-FRT (MANF mutants) or pTO-SH-GW-FRT as a control vector, 100 ng of plasmid/well using PEI Transfection Reagent (1 μg/μL in 1x PBS pH 4.5; 4:1 v/w ratio of PEI:DNA). 24 h after transfection, IRE1α-GFP expression was induced with doxycycline (1 μg/mL) treatment for 24 h. ER stress was induced by treating the cells with the inhibitor of N-linked glycosylation tunicamycin (TM), 5 μg/mL for 4 h. Thereafter, cells were fixed with 4% PFA for 20 min and stained with DAPI (D9542, Sigma-Aldrich) in 1 x PBS for 10 min. Imaging (16 sites/well) was performed using MolecularDevices Nano scanner. Three independent experiments were analyzed and quantified using CellProfiler 3.1.5 and CellProfiler Analyst 2.2.1 software.[71]

Western blot analysis

Western blot (WB) analysis for estimation of expression levels of Venus constructs of MANF, C-MANF and N-MANF was performed in HEK293 cells, plated 0.5× 10⁵ cells/well on 4-well dishes. 24 h after plating the transfection using JetPEI was performed according to manufacturer's instructions. 20 h after transfection the lysis was performed in RIPA buffer, containing protease inhibitor cocktail tablets (Roche). The concentrations of total protein in cell lysates were measured using NanoDrop 2000 spectrophotometer. 20 μg/well of total protein was loaded onto Bio-Rad mini-PROTEAN precast gels followed by the transfer onto nitrocellulose membrane. The transfer was performed for 1 h on ice at RT. The membranes were blocked in 5% BSA TBS-T (or 5% milk TBS-T) for 1 h at RT and then incubated with anti-Venus (Mybiosource, MBS448126) and α-Tubulin (Sigma-Aldrich, T9026) primary antibodies overnight at 4°C. Peroxidase-coupled secondary antibodies and the enhanced chemiluminescence (ECL) detection system were used for WB development.

WB analysis for estimation of IRE1α phosphorylation was performed in MEFs cells plated 2.5 × 10⁵ cells/well on 6-well plates in DMEM with 5% FBS and 1% non-essential amino acids. The next day the cells were treated with TM 500 ng/mL in DMEM without FBS for 4 h, and in the control group, the media was replaced with DMEM without FBS similarly to the treatment group. ER stress induction was followed by treatment with exogenous human recombinant MANF (50 nM) for 30, 60, and 240 min. The lysis was performed in RIPA buffer, containing protease and phosphatase inhibitor cocktail tablets (Roche). The concentrations of total protein measurement and WB was performed as described above. anti-IRE1α (CST, #3294), IRE1α pS724 (NovusBio, NB100-2323) and α-Tubulin (Sigma-Aldrich, T9026) primary antibodies were used.

Real-time quantitative PCR (RT-qPCR)

MEFs cells were plated 2.5 × 10⁵ cells/well on 6-well plates in DMEM with 5% FBS and 1% non-essential amino acids. Next day the cells were treated with TM 100 ng/mL for 4 h, followed by treatment with exogenous human recombinant MANF (150 nM) or MANF K96A (150 nM) for 20 h. The RNA was extracted using TRI reagent (Molecular Research Center). TRI reagent was added to the samples, incubated for 5 min, collected and chloroform (1:5) was added. The samples were centrifuged at 13000 rpm for 15 min, the aqueous phase of the samples was collected and mixed with isopropanol (1:1) and incubated for 10 min. Thereafter, the samples were centrifuged at 13000 rpm for 10 min and washed with 75% ethanol. After the centrifugation at 8000 rpm for 5 min the pellets were air-dried and dissolved in water. The concentrations of RNA were measured using NanoDrop 2000 spectrophotometer. 500 ng of each sample was used to synthesize complementary DNA. Maxima H Minus Reverse Transcriptase (EP0753, Thermo Fisher Scientific) in the presence of 10 mM dNTP mix (Fermentas UAB) and oligo-(dT) (Metabion International) was used to catalyze reverse transcription. qPCR was performed with Lightcycler 480 SYBR Green I Master mix (04887352001, Roche Diagnostics) using for measurements Lightcycler 480 Real-Time PCR System (Roche). The mRNA levels of the genes of interest were normalized to the mRNA levels of β-actin in corresponding samples. The primers used are listed in key resources table.

SCG neuronal culture microinjections

The nuclei of SCG neurons were then microinjected with the expression plasmid for full-length MANF (pTO-pre-SH-MANF) or MANF mutants together with a reporter plasmid for enhanced green fluorescent protein (EGFP), at total DNA concentration of 10 ng/μL in

each experiment. Neurons mock-injected with empty vector served as negative control. For protein microinjection, recombinant full length MANF protein (P-101-100, Icosagen) and mutant MANF proteins in PBS at 200 ng/μL was microinjected directly into the cytoplasm together with fluorescent reporter Dextran Texas Red (MW 70 kDa) (D1864, Invitrogen, Molecular Probes) that facilitates identification of successfully injected neurons. Control neurons were mock-injected with Dextran Texas Red without the proteins. Next day, TM (ab120296, Abcam) at the concentration of 2 μM was added. Living fluorescent (EGFP-expressing or Dextran Texas Red-containing) neurons were counted three days later and expressed as percentage of initial living fluorescent neurons counted 2–3 h after microinjection.

Immunocytochemistry

The neurons were cultured on glass coverslips and microinjected after 6–7 days *in vitro* with plasmid encoding for human wtMANF or its mutants at the DNA concentration of 10 ng/μL. The cells were fixed with 4% PFA at 24 h after microinjection and stained with the following antibodies: rabbit anti-MANF used in,[8] mouse anti-PDI (ADI-SPA-891-488F, Enzo Life Sciences), Alexa Fluor 488 goat anti-rabbit IgG (H + L) (A-11008, Invitrogen) and Alexa Fluor 568 goat anti-mouse IgG (H + L) (A-11004, Invitrogen). The nuclei were stained with DAPI (D9542, Sigma-Aldrich). The fluorescent image stacks were acquired using the confocal microscope TCS SP5 equipped with LAS AF 1.82 (Leica Microsystems Inc) with Leica HCX PL APO x63/1.3 GLYC CORR CS (21°C) objective. The lasers DPSS 561 nm/20 mW, OPSL 488 nm/270 mW and diode 405 nm/50 mW with the beam splitter QD 405/488/561/635 were used. The confocal images were analyzed by Imaris 9.2.1 software (Bitplane).

MANF treatment in primary cultures of midbrain dopamine neurons

After 5 days in culture the cells were treated with thapsigargin (20 nM) (T7458, Thermo Fisher Scientific) and wtMANF (100 ng/mL) or MANF K96A, MANF E153A and MANF R133E (10 ng/mL, 100 ng/mL, 1 μg/mL). After three days the neuronal cultures were fixed and stained with anti-Tyrosine Hydroxylase antibody (MAB318, Millipore Bioscience Research Reagents). Images were acquired by CellInsight high-content imaging equipment. Immunopositive neurons were counted and analyzed using CellProfiler 3.1.5 and CellProfiler Analyst 2.2.1 software.[71] The results are expressed as percentage of living neurons, compared with untreated neurons in the control wells.

RNA isolation, reverse transcription and quantitative RT-qPCR in dopamine neurons

E13 midbrain dopamine neurons were isolated and cultured for 5–7 days as described above and then treated with thapsigargin (200nM). Recombinant MANF protein (100 ng/mL) or MANF K96A (100 ng/mL) was added to the cultures at the same time. After 24 h RNA from cultured cells was isolated by TriReagent® (RT118, Molecular Research Center) according to manufacturer's instructions. RNA was reverse transcribed to cDNA with RevertAid^TM Premium Reverse Transcriptase (EP0441, Fermentas UAB, Thermo Fisher Scientific Inc). Quantitative PCR was performed using LightCycler® 480 SYBR Green I Master (04887352001, Roche Diagnostics GmbH) and Roche LightCycler® 480 Real-Time PCR System (Roche Diagnostics GmbH). The expression levels were normalized to the levels of β-actin in the same samples. Primers used in quantitative PCR were synthetized using previously published sequences[15] and listed in key resources table.

For the experiments with IRE1α inhibitors E13 midbrain dopamine neurons were isolated and cultured for 5–7 days as described and then treated with thapsigargin (200nM). Recombinant MANF protein (100 ng/mL) and IRE1α inhibitors 4μ8C (10 μM) or KIRA6 (200nM) were added to the culture medium at the same time. After 24 h RNA from cultured cells was isolated.

Testing MANF mutant in *in vivo* 6-OHDA model. 6-OHDA lesioning

6-OHDA injections were done under isoflurane anesthesia essentially as described earlier.[7,72,73] The animals received unilateral injections totaling 6 μg of 6-OHDA (Sigma Chemical CO, St. Louis, MO, USA; calculated as free base and dissolved in ice-cold saline with 0.02% ascorbic acid) in 3 deposits (2 μg / 1.5 μL each) in the right striatum using coordinates relative to the bregma (A/P + 1.6, L/M + 2.8, D/V −6; A/P 0.0, L/M +4.1, D/V −5.5 and A/P −1.2, L/M +4.5, D/V −5.5).[74] The rats were divided into treatment groups according to their amphetamine-induced rotations on two-week post lesion. After the behavioral tests, the rats were transcardially perfused and their brains were processed for TH immunohistochemistry.

Intrastriatal administration of compounds

MANF and mutant MANF were intrastriatally administered to 6-OHDA lesioned rats two weeks after lesioning under isoflurane anesthesia using the same stereotaxic coordinates as with 6-OHDA injections. MANF and mutant MANF were injected in three locations in the striatum in three injections of equal volume. The total injected doses of MANF and mutant MANF were 10 μg. The total injection volume was adjusted to be 2 μL for all compounds.

D-Amphetamine-induced rotational behavior was measured at 2, 4, 6 and 8 weeks post lesion in automatic rotometer bowls (Med Associates, Inc., Georgia, USA) as previously described.[45,75] Following a habituation period of 30 min, a single dose of D-amphetamine (2.5 mg/kg, Division of Pharmaceutical Chemistry, Faculty of Pharmacy, University of Helsinki, Finland) was injected intraperitoneally (i.p.). The rotation sensor recorded complete (360°) clockwise and counterclockwise-uninterrupted turns for a period of 2 h and ipsilateral rotations were assigned a positive value.

Immunohistochemistry

Perfusion and tissue preparations were done as described previously[7]: Rats were anesthetized with an overdose of sodium pento-barbital (90 mg/kg, i.p.; Orion Pharma) and perfused intracardially with PBS followed by 4% PFA in a 0.1 M sodium phosphate buffer, pH 7.4. The brains were removed, postfixed for 4 h, and stored in sodium phosphate buffer containing 20% sucrose at 4°C. Serial coronal frozen sections of 40 μm depth were cut on a sliding microtome.

Free-floating sections were processed for TH-immunohistochemistry as described above. After three rinses in PBS, endogenous peroxidase activity was quenched for 15 min in 0.3% H_2O_2 /PBS. After three rinses in PBS, the sections were pre-incubated with 0.3% Triton X-100/1% normal goat serum (S-1000, Vector Laboratories) in PBS to block nonspecific staining. Thereafter, sections were incubated overnight at RT with a 1:2000 dilution of rabbit anti-TH antibody (P40101-1, Pel-Freez Biologicals) or with a 1:1000 dilution of rat anti-DAT antibody (sc-32258, Santa Cruz). This was followed by incubation with a 1:400 dilution of biotinylated goat-anti-rabbit antibody (BA-1000, Vector Laboratories) or with goat anti-rat (BA-9400, Vector Laboratories) and with the avidin–biotin peroxidase complex using the Elite ABC Vectastain kit (Vector Laboratories). The reactions were visualized using 3, 3′-diaminoben-zidine (DAB) as a chromogen.

Morphological analyses

For the TH + cell analysis with deep neural network, the TH-stained tissue sections from substantia nigra area (AP -3.96 from bregma until AP -6.00 from bregma, 3–10 sections per rat) were digitized analyzed focus at resolution of 0.22 μm/pixel. The extended focus renders the whole section depth in a single focal plane. A total depth of 10 μm was acquired as five focal layers with 2 μm intervals. Next, the digitized images were uploaded to Aiforia image processing and management platform (Aiforia Oy, Helsinki, Finland) and analyzed using deep CNN algorithm and supervised learning. First, the CNN algorithm was trained to recognize TH-positive neuron cell bodies from the images in WebMicroscope.[76]

The optical density (OD) of the TH- and DAT-positive fibers in the striatum was analyzed from three coronal striatal sections from each rat. Every sixth section between AP +1.6 and AP +0.20 was cut on a cryomicrotome (Leica Instruments) and processed for TH immunohistochemistry. TH stained tissue sections were digitized using Panoramic P250 Flash II whole slide scanner (3DHistech, Budapest, Hungary) and fiber densities were measured using Image-Pro Plus software (version 3.0.1; Media Cybernetics). The OD analysis was performed under blinded conditions on coded slides. The data are presented as percentage of the intact side that was defined as 100%.

QUANTIFICATION AND STATISTICAL ANALYSIS

GraphPad Prism 7.0 software was used for statistical analysis. Statistical tests and sample sizes are indicated in the figure legends. A $p < 0.05$ was considered as statistically significant.